

Critic-Free Deep Reinforcement Learning for Maritime Coverage Path Planning on Irregular Hexagonal Grids

Carlos S. Sepúlveda^{a,b,*}, Gonzalo A. Ruz^{a,c,d}

^a*Facultad de Ingeniería y Ciencias, Universidad Adolfo Ibáñez, Av. Diagonal las Torres 2640, Santiago, Chile*

^b*Dirección de Programas, Investigación y Desarrollo, Armada de Chile, General del Canto 398, Valparaíso, Chile*

^c*Millennium Nucleus for Social Data Science (SODAS), Santiago, Chile*

^d*Millennium Nucleus in Data Science for Plant Resilience (PhytoLearning), Santiago, Chile*

Abstract

Maritime surveillance missions, such as search and rescue and environmental monitoring, rely on the efficient allocation of sensing assets over vast and geometrically complex areas. Traditional Coverage Path Planning (CPP) approaches depend on decomposition techniques that struggle with irregular coastlines, islands, and exclusion zones, or require computationally expensive re-planning for every instance. We propose a Deep Reinforcement Learning (DRL) framework to solve CPP on hexagonal grid representations of irregular maritime areas. Unlike conventional methods, we formulate the problem as a neural combinatorial optimization task where a Transformer-based pointer policy autoregressively constructs coverage tours. To overcome the instability of value estimation in long-horizon routing problems, we implement a critic-free Group-Relative Policy Optimization (GRPO) scheme. This method estimates advantages through within-instance comparisons of sampled trajectories rather than relying on a value function. Experiments on 1,000 unseen synthetic maritime environments demonstrate that a trained policy achieves a 99.0% Hamiltonian success rate, more than double the best heuristic (46.0%), while producing paths 7% shorter and with 24% fewer heading changes than the closest baseline. All three inference modes (greedy, stochastic sampling, and sampling with 2-opt refinement) operate under 50 ms per instance on a laptop GPU, confirming feasibility for real-time on-board deployment.

Keywords: Deep Reinforcement Learning, Coverage Path Planning, Maritime Surveillance, Hexagonal Grid, Neural Combinatorial Optimization, Maritime Domain Awareness

1. Introduction

Maritime surveillance (MS) underpins safety- and security-critical missions such as search and rescue (SAR), protection of critical infrastructure, prevention of illicit activities, and environmental monitoring (Boraz, 2009). Maritime transport carries the majority of global merchandise trade by volume, making the maritime domain a key component of national and international

*Corresponding author.

Email addresses: carlos.sepulveda@alumnos.uai.cl (Carlos S. Sepúlveda), gonzalo.ruz@uai.cl (Gonzalo A. Ruz)

resilience (United Nations Trade and Development (UNCTAD), 2024). Consequently, dense traffic, constrained chokepoints, and the strategic relevance of offshore infrastructure increase the operational demand for persistent Maritime Domain Awareness (MDA) (Bueger et al., 2024; Bischof et al., 2018).

Achieving MDA typically relies on heterogeneous sensing assets whose capabilities must be allocated over large areas of interest (AOIs) with limited endurance. This operational requirement gives rise to planning problems formalized as Coverage Path Planning (CPP) (Choset, 2001; Galceran and Carreras, 2013; Cabreira et al., 2019; Fevgas et al., 2022). CPP seeks trajectories that systematically observe an AOI under constraints on motion, endurance, and obstacles.

However, maritime environments present specific geometric challenges that complicate classical CPP. Realistic AOIs are rarely convex polygons; they frequently involve irregular coastlines, exclusion zones, islands, and navigational hazards (Nielsen et al., 2019; Mier et al., 2023). Standard sweep patterns (e.g., boustrophedon paths) typically require the exact cellular decomposition of the target area into simpler, sweepable sub-regions (Choset, 2001; Galceran and Carreras, 2013). This process relies heavily on the geometric morphology of the environment; irregular coastlines and dense exclusion zones generate numerous critical points that severely fragment the area. Consequently, routing a vehicle through these disjointed sub-regions becomes computationally intensive and kinematically inefficient, forcing excessive transit flights and sharp heading reversals (Cabreira et al., 2019; Nielsen et al., 2019). Furthermore, exact optimization-based approaches such as Mixed-Integer Linear Programming (MILP) or evolutionary algorithms typically solve each instance from scratch (Choi et al., 2019, 2020; Azad et al., 2017). This lack of generalization prevents the reuse of computational effort across different mission geometries, limiting their utility for rapid on-board replanning.

Reinforcement Learning (RL) offers a paradigm to learn policies that generalize across problem instances (Sutton and Barto, 2018; Kaelbling et al., 1996). In particular, attention-based Neural Combinatorial Optimization (NCO) has demonstrated that Transformer-based policies can learn to construct high-quality solutions for routing problems such as the Traveling Salesman Problem (TSP) (Kool et al., 2018; Berto et al., 2025). This paradigm is highly compatible with CPP over discretized AOIs, where the agent must select a sequence of nodes to visit. We adopt a hexagonal discretization due to its favorable geometric properties, such as equidistant neighbors and reduced anisotropy compared to grid maps (Boots et al., 1999; Kadioglu et al., 2019; Cho et al., 2021b).

In this work, we propose a Transformer-based pointer policy that operates on a graph representation of the hexagonal AOI. The policy constructs valid coverage tours by selecting feasible moves via dynamic action masking. A key innovation in our approach is the use of a critic-free Group-Relative Policy Optimization (GRPO) scheme. While Actor-Critic methods like Proximal Policy Optimization (PPO) are standard, learning an accurate value function for combinatorial problems with sparse rewards remains challenging. GRPO stabilizes training by estimating advantages from within-instance comparisons of multiple sampled trajectories (Shao et al., 2024), avoiding the bias and instability of a learned critic.

The main contributions of this work are:

- We formulate maritime CPP over irregular AOIs as a graph traversal problem on hexagonal grids with holes and obstacles, focusing on minimizing path length and turns while ensuring complete coverage.
- We design a Transformer-based pointer policy that constructs feasible coverage trajectories using validity masking, enabling the handling of variable-sized AOIs and arbitrary obstacle

configurations.

- We adapt GRPO to the CPP domain, demonstrating that critic-free learning via trajectory comparison is effective for stabilizing training in long-horizon routing tasks.
- We empirically demonstrate that a single learned policy generalizes to unseen geometries, achieving near-oracle feasibility rates and producing shorter, smoother paths than 13 classical heuristics without instance-specific retraining.

The remainder of the paper is organized as follows. Section 2 reviews related work. Section 3 formalizes the problem. Section 4 presents the proposed method and training scheme. Section 5 describes the experimental setup, Section 6 presents the results and discussion, and Section 7 concludes.

2. Related Work

This section reviews the lines of work most relevant to our formulation: (i) maritime surveillance and persistent monitoring, (ii) coverage path planning and hexagonal tessellations, and (iii) deep reinforcement learning for combinatorial routing. We close by positioning our approach within this landscape (visualized in Fig. 1).

2.1. Maritime surveillance and persistent monitoring

Maritime Domain Awareness (MDA) is a strategic requirement for safety and security missions, including search and rescue (SAR) and critical infrastructure protection (Boraz, 2009; Bueger et al., 2024). Traditional surveillance relies on heterogeneous sensor constellations like coastal radars, Automatic Identification System (AIS), and space-based assets, whose data must be fused into a consistent situational picture (Soldi et al., 2021; Dogancay et al., 2021). As national-level policy frameworks increasingly mandate persistent monitoring of vast maritime zones (de Ministros para el desarrollo de una Política Oceánica Nacional, 2023), the efficient scheduling and routing of mobile assets such as UAVs and USVs becomes operationally critical (Li and Savkin, 2021).

From an optimization perspective, maritime surveillance has been modeled as routing and mission-planning problems since at least the late 1990s: SAR mission planning as TSP variants (Panton and Elbers, 1999; John et al., 2001), regional platform routing for surface surveillance (Grob, 2006), and persistent aerial surveillance as mixed-integer linear programs (MILP) maximizing information gathered under endurance constraints (Zuo et al., 2020). Comprehensive surveys on UAV routing and trajectory optimization further highlight the complexity of integrating realistic vehicle dynamics, endurance constraints, and heterogeneous sensing objectives into tractable planning models (Coutinho et al., 2018; Otto et al., 2018). These contributions underline that, even before considering learning-based approaches, surveillance planning is inherently a high-dimensional combinatorial optimization problem.

2.2. Coverage path planning and hexagonal tessellations

CPP seeks a trajectory that visits every point in a region of interest while optimizing criteria such as path length or time (Galceran and Carreras, 2013). In maritime and aerial robotics, standard sweep patterns (e.g., boustrophedon) require decomposing complex areas into simpler

sub-regions (Choi et al., 2019; Nielsen et al., 2019), a process that is highly sensitive to the irregular morphology of coastlines and exclusion zones.

Hexagonal tessellations address this limitation: they minimize overlap and provide better isotropy than square grids, making motion costs direction-agnostic (Boots et al., 1999; Azpúrua et al., 2018). Hexagonal decompositions have been formulated in MILP models for multi-UAV maritime SAR (Cho et al., 2021b,a; Kadioglu et al., 2019), and the existence of Hamiltonian circuits in hexagonal grid graphs has been studied theoretically (Islam et al., 2007), establishing connectivity conditions directly relevant to complete-coverage feasibility. These results position hexagonal grids as a principled compromise between representational fidelity and algorithmic tractability.

Closely related are *sweep* and *barrier coverage* formulations, which focus on periodic traversal or boundary monitoring of target zones (Li et al., 2011; Benahmed and Benahmed, 2019). While historically addressed with static sensor deployments, these problems converge with CPP when mobile platforms (UAVs, USVs) are deployed to dynamically maintain coverage (Li et al., 2019).

2.3. Reinforcement learning and neural combinatorial optimization

Deep Reinforcement Learning (DRL) has been applied to enhance barrier and sweep coverage with mobile UAVs cooperating with sensor networks (Li and Chen, 2022), and more broadly to local ship maneuvering and collision avoidance (Gao et al., 2022), UAV path optimization under threat (Alpdemir, 2022), and dynamic maritime CPP using grid-based Markov decision processes (Ai et al., 2021; Wu et al., 2024). However, these controllers often rely on simple discretizations and small action spaces, struggling to scale to large, irregularly weighted grids.

A complementary paradigm is Neural Combinatorial Optimization (NCO), which treats DRL as a solver for routing problems. Starting with Pointer Networks (Vinyals et al., 2015), attention-based models have evolved into highly competitive solvers for TSP and Vehicle Routing Problems (Kool et al., 2018; Nazari et al., 2018; Berto et al., 2025). These graph RL policies operate directly on graph-structured inputs, learning construction heuristics that match exact solvers in quality while operating orders of magnitude faster at inference (Darvariu et al., 2024). Key advances include invalid-action masking for structured discrete spaces (Huang and Ontañón, 2022), and shared-instance baseline mechanisms such as POMO (Kwon et al., 2020), which drastically reduce gradient variance by comparing multiple rollouts from the same problem instance, an idea closely related to our critic-free GRPO training scheme (Shao et al., 2024).

2.4. Positioning of the present work

While CPP has been extensively studied (Cabreira et al., 2019) and maritime surveillance heavily relies on routing models (Zuo et al., 2020; Grob, 2006), few works explicitly address large-scale maritime CPP on hexagonal grids using learning-based combinatorial solvers. Existing barrier and sweep heuristics lack DRL integration, and attention-based NCO has rarely been applied to coverage topologies with geometric obstacles and sparse adjacency constraints.

Our work bridges this gap by modeling maritime surveillance as a CPP on a hexagonal grid, and tackling it with an attention-based DRL pointer policy trained via critic-free group-relative optimization. To synthesize the context reviewed above, Fig. 1 depicts a visual taxonomy of related problem families. A detailed breakdown of objectives and representative literature per category is provided in Table A.7 (Appendix Appendix A).

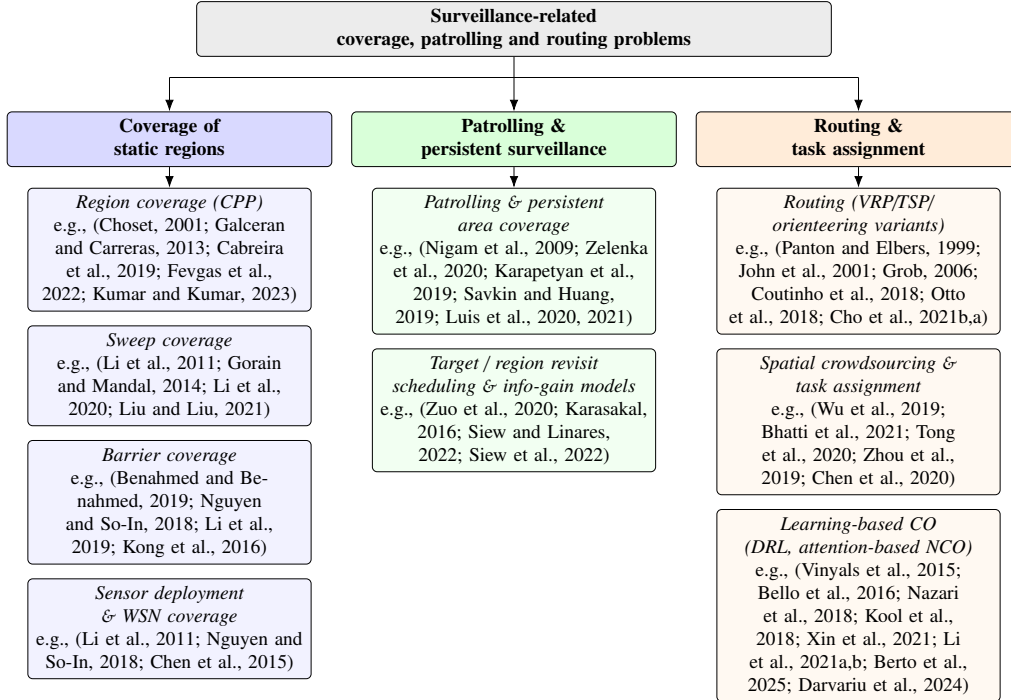


Figure 1: Taxonomy of surveillance-related coverage, patrolling, and routing problems underpinning our CPP formulation on hexagonal grids. The three columns mirror the structure of the *Related work* section, while Table A.7 provides a concise summary of the corresponding problem families.

3. Problem Formulation

3.1. Area of Interest and Coverage

Let the *area of interest* (AOI) be a planar polygonal region $\mathcal{P} \subset \mathbb{R}^2$ with a set of polygonal holes/obstacles $\{\mathcal{H}_k\}_{k=1}^K$. The feasible surveillance region is therefore

$$\mathcal{A} = \mathcal{P} \setminus \bigcup_{k=1}^K \mathcal{H}_k. \quad (1)$$

We consider a single mobile sensing platform whose planar position at discrete time $t \in \{0, \dots, T\}$ is $\mathbf{p}_t \in \mathcal{A}$.¹

Coverage path planning (CPP) is defined as generating a trajectory that guarantees *complete* or *persistent* sensing /visiting of a region under platform and sensors constraints (Choset, 2001; Galceran and Carreras, 2013; Cabreira et al., 2019; Fevgas et al., 2022; Tan et al., 2021).

In wide-area surveillance and reconnaissance, a standard abstraction is to model the instantaneous sensor footprint as a compact region around the platform position (often approximated

¹The formulation naturally extends to multiple platforms via task partitioning; this extension is discussed in Section 7.

by a disk), which aligns with classical geometric coverage models (e.g., unit-disk-type covering problems) Biniáz et al. (2017).

Accordingly, we model the effective footprint as a closed disk of radius $r_s > 0$,

$$\mathcal{F}(\mathbf{p}_t) = \{\mathbf{q} \in \mathbb{R}^2 : \|\mathbf{q} - \mathbf{p}_t\|_2 \leq r_s\}. \quad (2)$$

A point $\mathbf{q} \in \mathcal{A}$ is covered by a trajectory $\{\mathbf{p}_t\}_{t=0}^T$ if $\mathbf{q} \in \bigcup_{t=0}^T \mathcal{F}(\mathbf{p}_t)$. Directly optimizing trajectories over the continuous set \mathcal{A} is generally difficult, especially when \mathcal{A} is non-convex and includes holes; therefore CPP pipelines typically adopt cellular discretization to obtain a finite representation amenable to routing/optimization Choset (2001); Galceran and Carreras (2013); Cabreira et al. (2019); Fevgas et al. (2022). We adopt a hexagonal tessellation and graph construction pipeline detailed in Sections 3.3–3.4.

3.2. Why Approximate Discretizations

CPP literature distinguishes *exact* cellular decompositions (that preserve geometry with algorithmic guarantees) from *approximate* decompositions (grid/tessellation-based) Choset (2001); Galceran and Carreras (2013); Cabreira et al. (2019). Exact decompositions are attractive when one can exploit geometric structure, but they become cumbersome as the AOI grows in complexity (multiple holes, narrow passages) and when additional operational constraints must be incorporated (energy limits, risk maps, multi-vehicle coordination), often requiring repeated re-computation and complicated bookkeeping Cabreira et al. (2019); Fevgas et al. (2022); Tan et al. (2021). Approximate discretizations provide a controllable resolution parameter (cell size) that trades geometric fidelity for computational tractability, while enabling uniform neighborhood relations and direct mapping to graph-based routing formulations Cabreira et al. (2019); Fevgas et al. (2022); Tan et al. (2021). This trade-off is particularly relevant in maritime surveillance and other large-area missions where scalability and robustness are first-order requirements Grob (2006); Cabreira et al. (2019).

3.3. Hexagonal Tessellation of the AOI

We discretize \mathcal{A} by a hexagonal tessellation. In practice, we generate the grid in an oriented bounding box (OBB) frame to reduce boundary artifacts; the resulting tessellation-and-filtering sequence is illustrated in Fig. 2(a)–(c).

Let \mathcal{G}_h denote a regular hexagonal grid with characteristic size (e.g., circumradius) r_h . Hexagonal tessellations are a canonical class of spatial tessellations Boots et al. (1999) and have been used for coverage and surveillance planning due to their near-isotropic adjacency and reduced directional bias compared to square grids, which is beneficial when motion costs should be direction-agnostic Boots et al. (1999). Moreover, hexagonal decompositions have been explicitly adopted in UAV coverage and multi-UAV maritime SAR settings Kadioglu et al. (2019); Azpúrua et al. (2018); Cho et al. (2021b).

Beyond geometric convenience, hexagonal discretization is consistent with disk-like footprint abstractions: when coverage is approximated by disks, the discretization should avoid anisotropies that can distort effective coverage radii and neighborhood costs Biniáz et al. (2017); Boots et al. (1999). While the present work does not claim optimality of any single discretization, the above considerations motivate a hexagonal grid as a principled compromise between representational fidelity and algorithmic simplicity Boots et al. (1999); Cho et al. (2021b); Kadioglu et al. (2019); Azpúrua et al. (2018). In this pipeline, the hexagon size is selected to be

sensor-driven to align discretization resolution with the effective footprint. Specifically, the circumradius r_h of each hexagonal cell is set equal to the sensor footprint radius r_s , so that a single visit to a cell centroid guarantees coverage of the entire cell area. Consequently, the number of cells $|\mathcal{V}|$ is determined not by the absolute area of the AOI but by the ratio $\text{Area}(\mathcal{A})/\text{Area}(c)$ between the feasible region and the individual cell area, making the graph size scale-invariant.

Let $\mathcal{C} = \{c_1, \dots, c_N\}$ be the set of hexagonal cells whose interiors intersect \mathcal{A} , and let $\mathbf{s}_i \in \mathbb{R}^2$ be the centroid of cell c_i . Cells whose centroids fall inside holes are removed, yielding the feasible cell set

$$\mathcal{V} = \{i \in \{1, \dots, N\} : \mathbf{s}_i \in \mathcal{A}\}. \quad (3)$$

In practice, obstacles may be defined either as explicit polygonal holes \mathcal{H}_k or, equivalently, by directly removing selected cells from \mathcal{V} . Both approaches yield the same graph G ; the latter is used in our dataset generation for simplicity (Section 5.1).

Discrete coverage. We say cell c_i is *covered* at time t if the sensor footprint centered at \mathbf{p}_t contains its centroid \mathbf{s}_i :

$$\mathbf{1}\{c_i \text{ covered at } t\} = \mathbf{1}\{\|\mathbf{s}_i - \mathbf{p}_t\|_2 \leq r_s\}. \quad (4)$$

Under the common discretization assumption $\mathbf{p}_t \in \{\mathbf{s}_i\}_{i \in \mathcal{V}}$ (platform moves between cell centroids), coverage depends only on visited cells and can be represented combinatorially.

3.4. Graph Representation

The discretized AOI naturally induces a graph. Define an undirected adjacency relation $\mathcal{N}(i)$ over cells in \mathcal{V} such that $j \in \mathcal{N}(i)$ if cells c_i and c_j share an edge and the straight-line transition between \mathbf{s}_i and \mathbf{s}_j does not intersect any hole.² This yields a graph $G = (\mathcal{V}, \mathcal{E})$ with edges $\mathcal{E} = \{(i, j) : j \in \mathcal{N}(i)\}$. The edge construction from cell centers and the resulting AOI graph are depicted in Fig. 2(d)–(e). Let $c_{ij} \geq 0$ be the travel cost associated with moving from i to j (e.g., distance, time, or a risk-weighted metric). Graph abstractions of this form are standard in navigation and enable the use of graph-based reinforcement learning and combinatorial optimization techniques Darvari et al. (2024); Zweig et al. (2020).

A discrete path is a sequence $\pi = (v_0, v_1, \dots, v_T)$ with $v_t \in \mathcal{V}$ and $(v_t, v_{t+1}) \in \mathcal{E}$. Let $v_0 = b$ denote a designated base/initial cell (and optionally $v_T = b$ for return-to-base missions).

The base node b is positioned outside the tessellated AOI and connected to every cell on the outer ring of \mathcal{V} whose straight-line segment $\overline{b\mathbf{s}_i}$ does not intersect any obstacle. To represent the end of the mission, a duplicate terminal node b' is introduced, which in our current closed-loop experiments shares the exact same adjacency set. Architecturally, explicitly decoupling the departure and arrival nodes enables the framework to natively support open-path missions (e.g., launching from a mother ship and recovering at a distinct coastal base) by simply assigning distinct spatial coordinates and adjacency masks to b' , without requiring any modifications to the underlying neural policy. Finally, this line-of-sight constraint ensures that both departure and return transits safely avoid overflying exclusion zones.

²Additional edge-level constraints (e.g., no-go zones, directional restrictions) can be incorporated by removing or redirecting edges; the graph abstraction remains unchanged.

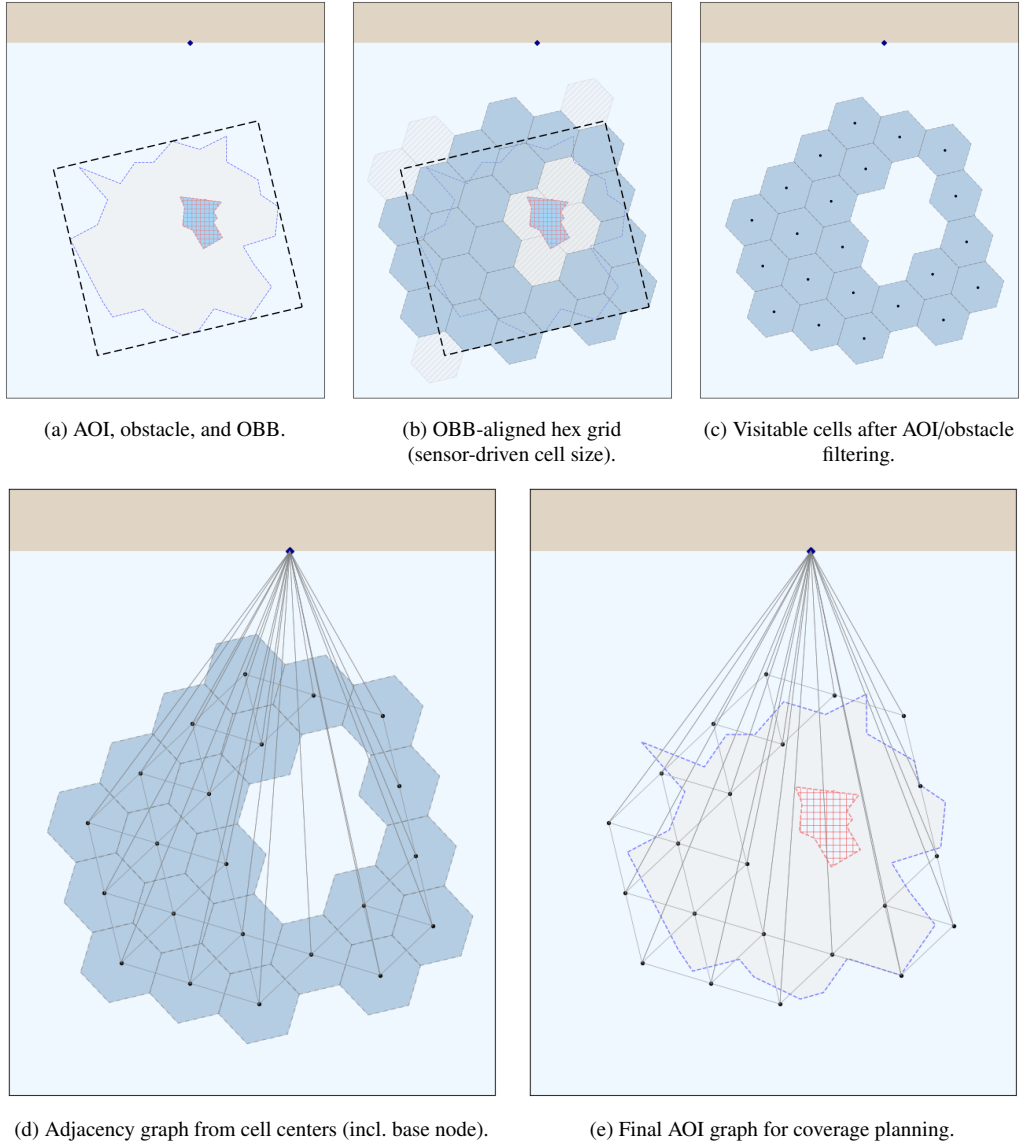


Figure 2: Hexagonal tessellation-to-graph pipeline for an irregular AOI with an internal obstacle. Hexagon size is set by the sensor footprint. (a) AOI, obstacle, and OBB. (b) OBB-aligned hex grid. (c) Visitable cells selected by intersection tests. (d) Graph edges defined by hex-neighborhood adjacency using cell centers (including the base node). (e) Final graph used for coverage planning. (The pipeline is illustrated with an explicit polygonal obstacle for visual clarity; in the experimental dataset, obstacles are implemented as individual cell removals—see Section 5.1.)

3.5. Combinatorial Optimization View: Relation to TSP/VRP

When coverage is enforced by visiting a set of discrete locations, CPP becomes closely related to routing problems such as TSP, vehicle routing problems (VRP), and their generalizations

(Bähmann et al., 2021; Raza et al., 2022). In the simplest complete-coverage case, one seeks a minimum-cost route that visits all required cells, which mirrors a Hamiltonian-path structure on the AOI graph.

However, the grid-based maritime CPP addressed here differs from the classical TSP in three operationally significant ways: (i) *sparse feasibility*: movements are restricted to local hexagonal adjacency rather than a fully connected graph, and irregular obstacle configurations can render certain node orderings infeasible; (ii) *kinematic costs*: heading changes incur maneuvering penalties that break the symmetry of Euclidean edge weights, coupling the cost of visiting a node to the direction of approach; and (iii) *dead-end risk*: unlike the classical TSP where every permutation of nodes constitutes a valid tour, the sparse and irregular topology of hex grids with obstacles means that certain visitation sequences lead to unrecoverable states from which complete coverage is impossible, making future feasibility non-trivial to assess without lookahead mechanisms.

Note that, by design, the hexagonal cell size is matched to the sensor footprint radius r_s (Section 3.3), so that complete area coverage requires visiting every cell in \mathcal{V} . This deliberately reduces the problem to a constrained Hamiltonian-path formulation on G , avoiding the additional complexity of partial-coverage models where sensing range exceeds cell size. Extensions to non-uniform coverage priorities and multi-vehicle coordination, while operationally relevant, are beyond the scope of this work and are discussed in Section 7.

3.6. Markov Decision Process Formulation

While the CPP problem can be naturally formulated as a MILP targeting the Hamiltonian path, exact solvers become computationally intractable for grids scaling beyond approximately $N \approx 15$ nodes due to the NP-hard nature of the underlying routing constraints (Cho et al., 2021b; Zuo et al., 2020). In maritime scenarios requiring rapid replanning over complex areas, relying on solvers that scale exponentially is operationally unfeasible. We therefore cast the coverage path planning on the AOI graph $G = (\mathcal{V}, \mathcal{E})$ as a finite-horizon Markov decision process (MDP) solved via DRL.

State. Each node $i \in \mathcal{V}$ carries geometric features (normalized centroid coordinates) and a nonnegative priority weight w_i (*hexscore*). The state at step t comprises: (i) the current node v_t , (ii) the set of already visited nodes $\mathcal{S}_t \subseteq \mathcal{V}$, represented as a binary mask, and (iii) the static instance data $(G, \{w_i\})$. This state representation allows the MDP formulation to natively support both uniform coverage path planning ($w_i = 0$ for all i) and priority-weighted coverage ($w_i \geq 0$ drawn from a spatial distribution). While the neural architecture fully integrates these priority maps, the experiments in this paper isolate the geometric routing challenge by focusing exclusively on the uniform coverage case; heterogeneous priority fields are deferred to future work.

Actions and feasibility masking. The action a_t selects the next node v_{t+1} among the unvisited feasible neighbors of v_t :

$$a_t \in \mathcal{A}(s_t) = \{j \in \mathcal{N}(v_t) : j \notin \mathcal{S}_t\}, \quad (5)$$

where $\mathcal{N}(v_t)$ denotes the graph neighborhood of v_t . Invalid actions are prevented by applying an additive mask to the policy logits before the softmax activation. This technique has been shown to preserve valid policy gradients while strictly outperforming penalty-based constraints in discrete action spaces (Huang and Ontañón, 2022). Crucially, our mask enforces two strict topological

rules: (1) it assigns $-\infty$ to non-neighbors and already-visited nodes to guarantee dynamically feasible, self-avoiding paths, and (2) it explicitly masks the terminal base node until 100% of the target cells have been visited. This terminal-masking prevents the agent from exploiting early-return behaviors to minimize kinematic costs, forcing it to navigate the entire region before it can extract the episodic completion reward.

Terminal conditions. An episode terminates in one of two ways: (i) *successful completion*, when the agent has visited all target cells and returned to the base node, receiving a large positive reward; or (ii) *dead-end failure*, when no unvisited neighbor is reachable, in which case a penalty is applied. This latter condition is common in irregular hex grids where narrow passages and obstacles create geometric choke points. We address it with a Breadth-First Search (BFS) look-ahead mechanism described in Section 4.3.

Reward function. The total return of a trajectory π of length T is:

$$R(\pi) = \sum_{t=0}^{T-1} \left(r_{step}^{(t)} + r_{hex}^{(t)} - c_{dist}^{(t)} - c_{turn}^{(t)} \right) + R_{episodic}, \quad (6)$$

where the dense components are evaluated at each transition (v_t, v_{t+1}) , and $R_{episodic}$ is a terminal modifier. The reward components, calibrated to prevent degenerate behaviors such as premature termination or redundant looping, are summarized in Table 1.

Table 1: Dense and episodic components of the reward function.

Component	Value	Type	Operational justification
r_{step}	+2.0	Dense	Incentive per newly visited hexagonal cell.
r_{hex}	+0.5 · w_{v_t}	Dense	Time-decayed priority bonus for early visitation of high-value zones (inactive in uniform-coverage experiments) [†] .
c_{dist}	-1.0 · \bar{d}	Dense	Penalty proportional to normalized inter-cell distance.
c_{turn}	-0.25 · $f(\theta)$	Dense	Kinematic penalty for sharp heading changes, promoting smooth trajectories.
$r_{complete}$	+100.0	Episodic	Sparse reward for full coverage and return to base.
r_{death}	-40.0	Episodic	Penalty for falling into an unrecoverable geometric dead-end.

[†] The hexscore channel w_i is architecturally supported but set to zero in all reported experiments (Section 5.1).

Here, the normalized distance $\bar{d}_t = \|\mathbf{s}_{v_t} - \mathbf{s}_{v_{t+1}}\|_2 \cdot \sqrt{|\mathcal{V}|}$ scales the inter-cell Euclidean distance by a density factor that normalizes the penalty across instances of varying size, ensuring that larger grids do not trivially dominate the cost structure. The turn penalty $f(\theta_t)$ is a composite function of the heading change angle $\theta_t \in [0, \pi]$ between consecutive movement vectors. To reflect the physical reality of maritime vehicles, where initiating a course change involves a fixed mechanical overhead (e.g., rudder actuation) plus an angle-dependent hydrodynamic resistance, the penalty combines a discrete activation cost and a quadratic magnitude cost:

$$f(\theta_t) = \begin{cases} 2 \left[\left(\frac{\theta_t}{\pi} \right)^2 + c_{base} \right] & \theta_t > 0, \\ 0 & \theta_t = 0, \end{cases} \quad (7)$$

where c_{base} is a constant maneuvering penalty. In our implementation, we empirically calibrate $c_{base} = 1/12$. This specific value ensures that for the minimum required course correction on a hexagonal grid (60°), the fixed mechanical overhead ($1/12 \approx 0.083$) and the quadratic dynamic resistance ($(1/3)^2 \approx 0.111$) are of comparable magnitude, appropriately reflecting the high inertia and rudder-shift costs of maritime platforms. For larger maneuvers, the quadratic term naturally dominates. Because the minimum non-zero heading change is 60° , every maneuver robustly activates this full penalty structure. Straight-line motion ($\theta_t = 0$) and the first step of each episode incur no turn cost. Consequently, the fixed term heavily penalizes the total *number* of turns, while the quadratic term strictly limits sharp reversals, explicitly discouraging zigzagging and promoting dynamically smooth trajectories.

The objective is to learn a stochastic policy $\pi_\theta(a_t | s_t)$ that maximizes the expected return $\max_\theta \mathbb{E}_{\pi_\theta}[R(\pi)]$ over a distribution of irregular AOI geometries.

4. Proposed Method

This section describes the three components of our approach: (i) a Transformer-based pointer policy that constructs coverage tours autoregressively (Section 4.1), (ii) a critic-free GRPO training scheme that avoids learning a value function (Section 4.2), and (iii) an early dead-end detection mechanism that accelerates convergence on irregular grids (Section 4.3). We close with a description of the training procedure, including data generation and augmentation (Section 4.4).

4.1. Transformer-based pointer policy

Our policy follows the attention-based neural combinatorial optimization paradigm (Kool et al., 2018; Berto et al., 2025): an encoder produces contextual node embeddings for the AOI graph, and an autoregressive decoder *points* to the next node to visit. The full architecture is depicted in Fig. 3.

Node features and embedding. Each node $i \in \mathcal{V}$ is represented by a feature vector $\mathbf{x}_i = [x_i, y_i, w_i, m_i]$. To ensure the policy generalizes robustly across AOIs of varying absolute physical dimensions, the spatial coordinates (x_i, y_i) are centered at the base node and normalized by the maximum radial extent of the graph within the instance. w_i is the hexscore priority, and m_i is a binary indicator identifying the base node. A learnable linear projection maps \mathbf{x}_i to an initial embedding $\mathbf{h}_i^{(0)} \in \mathbb{R}^d$.

Graph-aware encoder. A multi-layer Transformer encoder exchanges information across nodes. To respect the sparse structure of the hex graph, attention is restricted to k -hop neighborhoods using the adjacency matrix as a mask, yielding graph-structured self-attention. After L layers, we obtain contextual embeddings $\mathbf{h}_i = \mathbf{h}_i^{(L)}$ and a global graph embedding $\bar{\mathbf{h}} = \frac{1}{|\mathcal{V}|} \sum_i \mathbf{h}_i$.

Autoregressive decoder. At step t , the decoder constructs a context-aware query from four sources: (i) the embedding of the current node v_t , (ii) the embedding of the first node v_0 , (iii) the global graph embedding $\bar{\mathbf{h}}$, and (iv) a set of environmental signals encoding coverage progress, heading direction, frontier statistics, and reachability status. These signals are projected to the model dimension and concatenated before passing through a context network (two-layer MLP with residual connection) that produces the decoder output $\mathbf{q}_t \in \mathbb{R}^d$.

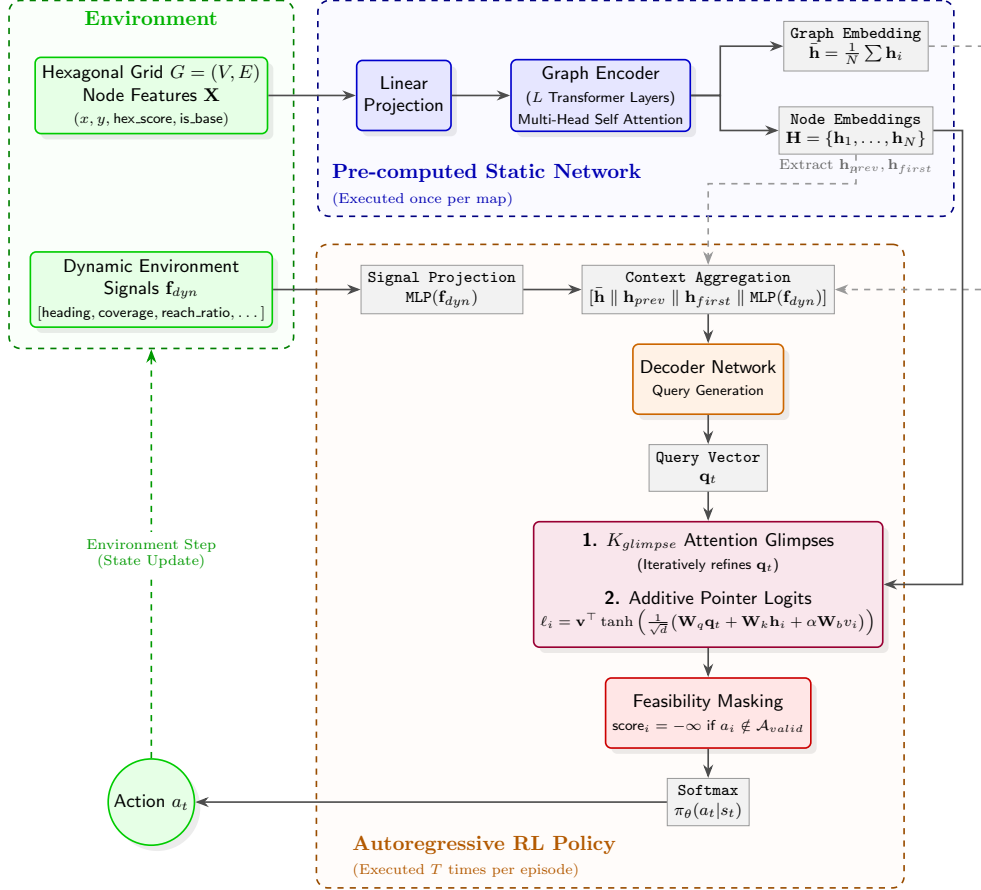


Figure 3: Proposed Transformer-based pointer policy for coverage path planning. The Graph Encoder pre-computes static node embeddings, while the Decoder dynamically aggregates the agent’s spatial context and environmental signals to generate a query. The Pointer Network computes attention scores over valid nodes, strictly constrained by a feasibility mask to guarantee valid routing.

Pointer mechanism with masking. The decoder output attends to the key projections of all node embeddings through $K_{glimpse}$ attention glimpses (Kool et al., 2018), iteratively refining the query vector \mathbf{q}_t . The final logits are computed via additive (Bahdanau-style) attention with a tanh activation and a learnable projection vector \mathbf{v} :

$$\ell_{i(j)} = \mathbf{v}^\top \tanh\left(\frac{1}{\sqrt{d}}(\mathbf{W}_q \mathbf{q}_t + \mathbf{W}_k \mathbf{h}_j + \alpha \mathbf{W}_b v_j)\right), \quad (8)$$

where $v_j \in \{0, 1\}$ encodes the visitation status of node j , α is a learnable gating scalar mapping the binary status into the continuous embedding space, and $\mathbf{W}_q, \mathbf{W}_k, \mathbf{W}_b$ are learnable weight matrices. An additive action mask $\mathcal{M}_t(j) \in \{-\infty, 0\}$ enforces feasibility:

$$\pi_\theta(a_t = j | s_t) = \text{softmax}\left(\text{clip}(\ell_{i(j)} + \mathcal{M}_t(j), C)\right)_j, \quad (9)$$

where $C > 0$ is a tanh clipping constant that bounds logit magnitudes. The mask assigns $-\infty$ to non-neighbors and already-visited nodes, ensuring that all sampled trajectories are feasible by construction. During training, actions are sampled from the categorical distribution. For evaluation during the training phase (validation), greedy decoding is used exclusively to strictly monitor policy convergence. At test time, however, the trained policy supports multiple decoding strategies of varying computational cost to trade off latency for path quality, as detailed in Section 5.3.

While some attention-based routing models employ scaled dot-product mechanisms for the final pointer logits (Kool et al., 2018), we adopt an additive (Bahdanau-style) attention head following the original Pointer Network formulation (Vinyals et al., 2015; Bello et al., 2016). The additive attention evaluates the compatibility between the decoder’s query and the candidate keys through a non-linear projection (tanh), acting effectively as a single-hidden-layer Multi-Layer Perceptron. This non-linearity provides greater expressive capacity to capture complex geometric relationships between the agent’s current state and the surrounding irregular grid. Furthermore, the intrinsic saturation of the inner tanh function naturally bounds the pre-logit activations. Combined with the outer clipping parameter C , this architectural choice significantly enhances numerical stability during policy gradient updates, preventing premature entropy collapse and maintaining healthy exploration in the early stages of training.

Complexity. With neighbor-restricted attention, encoder complexity scales as $O(|\mathcal{V}| \cdot d_{max} \cdot d^2)$ per layer, where d_{max} is the maximum node degree (at most 6 for hexagonal grids). Decoding is $O(|\mathcal{V}| \cdot d^2)$ per step. This is advantageous for large AOIs compared to full-attention Transformers that scale quadratically in $|\mathcal{V}|$.

4.2. Critic-free Group-Relative Policy Optimization

Standard actor-critic methods such as PPO (Schulman et al., 2017) require learning a value function $V_\phi(s)$ to estimate advantages. In combinatorial routing, the value function must generalize across highly diverse graph topologies with sparse terminal rewards, which often leads to high bias and training instability. Shared-instance baseline mechanisms, such as POMO (Kwon et al., 2020), mitigate this by evaluating multiple parallel trajectories constructed from diverse starting nodes, using their average return as an instance-specific baseline.

Because our maritime CPP formulation models missions deploying from a fixed base node, we cannot exploit starting-node symmetries. Instead, we adapt this shared-baseline principle through GRPO (Shao et al., 2024). For each training instance n , we sample a group of G trajectories $\{\pi_n^{(g)}\}_{g=1}^G$. To guarantee constructive diversity across the group despite the single fixed starting node, we rely on the policy’s stochastic categorical sampling, which is heavily promoted during early training via a high initial temperature annealing schedule ($T_{init} = 1.5 \rightarrow 1.0$). We then compute the relative advantages by standardizing the episodic returns (Eq. 6) within the group:

$$A_n^{(g)} = \frac{R_n^{(g)} - \mu_n}{\sigma_n + \epsilon}, \quad (10)$$

where $\mu_n = \frac{1}{G} \sum_g R_n^{(g)}$, $\sigma_n = \sqrt{\frac{1}{G} \sum_g (R_n^{(g)} - \mu_n)^2}$, and ϵ is a small constant for numerical stability. This formulation evaluates whether a trajectory outperformed its peers on the exact same map, effectively bypassing the generalization bottleneck of a global critic network.

The policy is then optimized via a clipped surrogate objective applied at the *per-step* level. Let $r_t(\theta) = \pi_\theta(a_t | s_t) / \pi_{\theta_{\text{old}}}(a_t | s_t)$ be the importance-sampling ratio for action a_t . The GRPO loss is:

$$\mathcal{L}_{\text{GRPO}}(\theta) = -\frac{1}{|\mathcal{T}|} \sum_{(n,g,t) \in \mathcal{T}} \min \left(r_t(\theta) A_n^{(g)}, \text{clip}(r_t(\theta), 1 - \varepsilon, 1 + \varepsilon) A_n^{(g)} \right) - \beta \bar{\mathcal{H}}, \quad (11)$$

where \mathcal{T} denotes the set of valid (non-padding) tokens across all trajectories, ε is the clipping parameter, $\bar{\mathcal{H}}$ is the mean per-step policy entropy, and β is the entropy coefficient. The per-step formulation, as opposed to per-trajectory clipping, ensures that the trust region constraint is enforced at each decision point, which is critical for long-horizon routing where per-trajectory ratios can grow exponentially with sequence length.

Multi-epoch reuse. For each batch of B instances with G rollouts each, we perform K inner optimization epochs over shuffled minibatches, re-evaluating log-probabilities and entropy under the current policy parameters at each step. This is analogous to the inner-loop structure of PPO, and provides substantial sample efficiency compared to single-update REINFORCE methods.

4.3. Early dead-end detection via BFS

On irregularly shaped hexagonal grids, narrow passages, peninsulas, and obstacle configurations frequently create situations where the agent, having visited certain nodes, can no longer reach all remaining targets—a *geometric dead-end*. Without early detection, the agent continues making decisions along a doomed trajectory, receiving misleading intermediate rewards before eventually triggering the terminal death penalty. This contaminates credit assignment: the policy cannot distinguish between the critical misstep that created the dead-end and the subsequent (irrelevant) actions.

We integrate a Breadth-First Search (BFS) reachability check into the environment. At each step t , after the agent moves to node v_t , the BFS computes the set of unvisited nodes reachable from v_t through unvisited (or transit-eligible) intermediate nodes, and verifies whether the terminal base node remains accessible. If either condition fails, i.e., some target nodes or the base are unreachable, the episode is terminated immediately with the death penalty r_{death} .

This mechanism provides two benefits:

1. **Sharper credit assignment.** The penalty is applied at the step where the dead-end becomes inevitable, rather than many steps later. The policy gradient correctly attributes the negative outcome to the responsible decision.
2. **Reduced wasted computation.** Doomed trajectories are truncated early, freeing rollout budget for informative trajectories. Empirically, enabling BFS detection substantially reduces the fraction of non-informative rollouts during early training, allowing the policy gradient to receive meaningful credit-assignment signal from the first epoch.

The BFS has worst-case complexity $\mathcal{O}(|\mathcal{V}| + |\mathcal{E}|)$ per step. For hex grids with $|\mathcal{V}| \leq 46$ and $|\mathcal{E}| \leq 6|\mathcal{V}|$, this overhead is negligible compared to the Transformer forward pass.

4.4. Training procedure

Dataset generation. Training and evaluation use a synthetic dataset of 10,000 irregular hexagonal AOI instances ($|\mathcal{V}| \in [28, 46]$) with stochastic cell-level obstacle patterns; the generation procedure and morphological families are described in Section 5.1.

Geometric augmentation. During training, each batch undergoes stochastic geometric augmentation with probability $p_{aug} = 0.9$: random rotations, reflections, and coordinate permutations are applied to the AOI graph. This exposes the policy to geometric invariances and significantly improves generalization to unseen AOI shapes without increasing the dataset size.

Temperature annealing. To balance exploration and exploitation, sampling temperature is linearly annealed from $T_{init} = 1.5$ to $T_{final} = 1.0$ over the first 10 epochs. Higher initial temperature encourages diverse trajectory exploration during early training, while convergence to unit temperature ensures that the final policy is evaluated under standard softmax probabilities.

Hyperparameters. The full training configuration is summarized in Table 2. Key choices include $G = 16$ rollouts per instance (balancing baseline quality against computational cost), $K = 4$ inner PPO-style epochs per batch, a learning rate of 3×10^{-5} with linear annealing, and an entropy coefficient of $\beta = 0.02$.

Table 2: Training hyperparameters.

Parameter	Description	Value
d	Model dimension	128
L	Encoder layers	3
n_h	Attention heads	8
$K_{glimpse}$	Decoder glimpses	2
G	Rollouts per instance	16
K	Inner optimization epochs	4
ε	PPO clip parameter	0.2
β	Entropy coefficient	0.02
lr	Learning rate	3×10^{-5}
–	LR schedule	Linear annealing
B	Batch size (instances)	32
B_{mb}	Minibatch size (trajectories)	8
–	Optimizer	Adam
$\ \nabla\ $	Max gradient norm	0.5
–	Max epochs (early stop at 30)	300
–	Augmentation probability	0.9
T_{init}/T_{final}	Temperature annealing	1.5 / 1.0
–	Early dead-end detection	Enabled

5. Experimental Setup

5.1. Dataset description

Training instances are generated synthetically to represent a range of maritime AOI morphologies. Each instance is constructed in three stages: (i) an irregular polygon is sampled to

define the outer boundary of the AOI, (ii) a hexagonal tessellation is applied with cell circumradius $r_h = r_s$ matching the sensor footprint (Section 3.3), and (iii) a subset of interior cells is randomly removed to simulate islands, shoals, or other navigational exclusion zones. This cell-level obstacle generation is mathematically equivalent to inscribing small polygonal holes within the AOI and discarding any hexagon whose centroid falls inside them, but operates directly on the graph topology without requiring explicit geometric intersection tests.

The outer polygons are drawn from three morphological families representing common maritime scenarios: (i) compact convex regions (open-water patrol zones), (ii) elongated or concave polygons (coastal strips, fjords, channel approaches), and (iii) irregular shapes with narrow passages created by the interaction of boundary concavities and internal cell removals. The combination of polygon shape and stochastic cell removal produces a wide spectrum of graph topologies, including bottlenecks, peninsulas, and disconnected-looking corridors that are characteristic of real maritime environments with islands and reefs.

Since the number of visitable cells $|\mathcal{V}|$ depends on the ratio between the AOI area and the cell area (Section 3.3), the geometric bounds of our dataset were rigorously calibrated to reflect real-world maritime domain parameters. We generate operational areas ranging from 1,600 to 3,600 square nautical miles (NM²). Crucially, by constraining the total area rather than bounding box dimensions, the generator naturally accommodates highly diverse morphologies under the same operational footprint, spanning from compact open-water Search and Rescue (SAR) sectors to elongated coastal patrol corridors. The cell circumradius is sampled between 5.0 and 7.0 NM, explicitly matching the effective detection horizon of an X-band marine radar on a medium-sized Autonomous Surface Vehicle (ASV) or the EO/IR footprint of a tactical UAV. Additionally, the base node is stochastically placed at a standoff distance of 100 to 250 NM, simulating the realistic offshore transit from a coastal naval base or a mother ship.

By driving the tessellation strictly through these doctrinal operational capabilities, the resulting spatial graphs consistently emerge with $|\mathcal{V}| \in [28, 46]$ valid target cells. This demonstrates that instances of this topological scale are not merely mathematical abstractions, but rather the exact combinatorial resolution required to plan persistent surveillance missions for modern maritime assets.

A total of 10,000 instances are generated and partitioned into 8,000 training, 1,000 validation, and 1,000 test instances. Polygon vertices, cell removal patterns, and base-node locations are sampled randomly subject to connectivity constraints ensuring that the resulting graph remains connected.

Hamiltonian-path feasibility audit. Since our formulation requires visiting every cell exactly once (Section 3.5), it is essential that every instance in the dataset admits at least one feasible Hamiltonian path. We verify this exhaustively using a depth-first search with strict backtracking over the full graph. All 10,000 instances pass this audit. Consequently, the exhaustive DFS serves as a *feasibility oracle* confirming a 100% theoretical solve rate. However, because DFS merely finds the first valid topological sequence without optimizing kinematic costs or distance, its path quality is generally poor. Therefore, it is utilized strictly as a ground-truth upper bound for feasibility, not as a target benchmark for path optimization.

In the experiments reported here, all instances use uniform coverage priority ($w_i = 0$ for all $i \in \mathcal{V}$), reducing the objective to minimum-cost complete coverage. The architecture natively supports non-uniform priorities via the hexscore input channel; experiments with heterogeneous priority fields are deferred to future work (Section 7).

5.2. Baseline methods

To evaluate the learned policy against a broad spectrum of classical CPP strategies, we implement 13 heuristic baselines spanning six algorithmic families. All baselines operate on the same hexagonal grid graph under identical adjacency constraints. However, a crucial methodological distinction exists regarding visitation constraints. While our RL policy is strictly constrained to single-visit paths via its action masking (terminating an episode if a dead-end is reached), classical heuristic baselines may traverse previously visited nodes (via backtracking, flyback transit, or overlapping sweeps) as a natural consequence of their construction logic, thereby achieving complete area coverage at the cost of redundant motion. This difference highlights a fundamental operational trade-off: traditional heuristics guarantee 100% coverage completion at the cost of inefficient overlapping paths, whereas our learned policy prioritizes maximum kinematic and distance efficiency by attempting to solve the stricter Hamiltonian path variant. The families and their members are summarized in Table 3.

The six families represent fundamentally different algorithmic paradigms in CPP: geometric decomposition (sweep families), morphology-following (contour/spiral), topological coverage guarantees (STC), local graph heuristics, and space-filling curves. This diversity ensures that performance comparisons are not biased toward any single planning philosophy.

5.3. Inference strategies

Unlike classical exact solvers that compute a single solution, generative routing models allow multiple decoding strategies at inference time. We evaluate the trained policy on the test set using three modes that trade computational cost for solution quality:

1. **Greedy (RL-Greedy):** At each step, the node with the highest logit is selected deterministically. This provides single-pass, lowest-latency inference ($O(|V|)$ steps).
2. **Best-of- K sampling (RL-BoK):** K independent trajectories are sampled in parallel from the stochastic policy. We select the trajectory that successfully completes the Hamiltonian path with the highest episodic return (i.e., minimum kinematic and distance cost). If no trajectory achieves strict complete coverage (i.e., all K rollouts reach a geometric dead-end before visiting every cell), we employ a robust fallback logic: the model outputs the partial trajectory that maximizes the total covered area before failure, breaking ties by minimum distance. Thanks to GPU batching, generating $K = 16$ parallel rollouts is computationally efficient and only marginally slower than greedy decoding.
3. **Best-of- K with local search (RL-BoK+2opt):** The best sampled trajectory is refined via a 2-opt local search that iteratively reverses sub-segments of the tour to untangle crossings, accepting improvements in total path cost. Crucially, because the environment is a sparse graph and not a fully connected Euclidean space, feasibility (strict adjacency and single-visit constraints) is explicitly verified after each proposed reversal. This demonstrates the seamless integration of neural construction heuristics with classical refinement.

The RL-BoK and RL-BoK+2opt variants are then applied only at test time to the selected trained model and should therefore be interpreted as inference-time enhancements rather than separately trained policies.

5.4. Evaluation metrics

To capture the trade-off between guaranteed coverage, path efficiency, and computational latency, we evaluate all methods along five dimensions:

Table 3: Baseline heuristic methods grouped by algorithmic family. All methods operate on the same hex-graph representation under identical constraints.

Family	Method	Description
Linear sweep (Boustrophedon)	<code>sweep_boustrophedon</code>	Classic lawnmower pattern with alternating row directions, minimizing inter-row transit.
	<code>sweep_row_oneway</code>	Unidirectional row sweep; all rows traversed in the same direction with flyback transit.
	<code>sweep_segment_snake</code>	Obstacle-aware boustrophedon that decomposes the AOI into convex segments and applies snake patterns within each.
Interleaved sweep (Skip-row)	<code>sweep_row_interleave</code>	Skips rows to allow wider turning arcs; rows are visited in an interleaved order (e.g., 1, 7, 2, 8, ...).
	<code>sweep_segment_interleave</code>	Combines segment decomposition with interleaved row ordering for kinematically constrained vehicles.
Contour / Spiral (Boundary rings)	<code>boundary_spiral_inward</code>	Traces concentric rings from the AOI perimeter inward toward the centroid.
	<code>boundary_spiral_outward</code>	Starts at the centroid and spirals outward to the perimeter.
	<code>sweep_boundary_peel</code>	Iteratively erodes the outermost layer of unvisited cells, adapting dynamically if the remaining area splits.
Spanning-tree coverage (STC)	<code>stc_tree_coverage</code>	Builds a minimum spanning tree over grouped cells; the agent circumnavigates the tree edges.
	<code>stc_like</code>	Adapted STC for hex grids with mandatory start/end nodes, using BFS to connect dead branches.
Graph-based local search	<code>warnsdorff</code>	Adapts the Knight’s Tour heuristic: always moves to the unvisited neighbor with the fewest remaining neighbors, clearing difficult corners first.
	<code>dfs_backtrack</code>	Depth-first greedy traversal with shortest-path backtracking when a dead-end is reached.
Space-filling curve	<code>morton_zorder</code>	Orders cell centroids by their Morton code (bit-interleaved coordinates), producing a Z-order curve that preserves spatial locality.

1. **Hamiltonian Success Rate (HSR, %)**: the fraction of test instances for which a method produces a valid start-to-terminal path that visits every required node exactly once. For the proposed RL policy, this is the primary success criterion. For classical baselines, this metric indicates whether their output happens to satisfy the stricter Hamiltonian requirement, even though they were not designed for it.
2. **Coverage Completion Rate (CCR, %)**: the fraction of test instances for which all re-

quired nodes are covered and the terminal node is reached, regardless of revisits. This reflects the native operating regime of classical coverage heuristics.

3. **Node Revisits:** the average number of previously visited nodes traversed during the generated route. This measures the overlap cost incurred by revisit-allowed strategies. By construction, the proposed RL policy yields zero revisits on instances counted as Hamiltonian successes.
4. **Normalized Path Distance:** the total Euclidean route length normalized by the characteristic inter-cell spacing. To isolate route quality from outright feasibility, this metric is reported conditionally on the pairwise common solved subset between the compared methods.
5. **Number of Turns:** the number of non-zero heading changes along the route. As with normalized distance, this metric is reported on the pairwise common solved subset in order to compare route quality independently of failure cases.

For the main route-quality comparison, we use the subset

$$\mathcal{I}_{\cap}^{(m)} = \{i \in \mathcal{D}_{test} \mid \text{RL-BoK+2opt solves } i \text{ under HSR} \\ \text{and baseline } m \text{ completes } i\},$$

and compute distance and turn metrics only on $\mathcal{I}_{\cap}^{(m)}$. This conditional analysis should be interpreted as a comparison of route quality on matched instances, not as a substitute for global feasibility metrics.

5.5. Implementation details

All experiments were conducted under Windows Subsystem for Linux 2 (WSL2) running Ubuntu 24.04.4 LTS on a workstation equipped with an AMD Ryzen 9 5900HX CPU, 31 GiB of system RAM, and an NVIDIA GeForce RTX 3070 Laptop GPU (8 GB VRAM). The software stack utilized Python 3.12.2, PyTorch 2.4.0, and CUDA 12.4.

The neural policy comprises approximately 2.05 million trainable parameters. Training was configured for up to 300 epochs with early stopping (patience of 4 epochs on validation success rate); the best checkpoint was selected at epoch 30 (val. SR = 95.5%), after which validation performance began to decrease while training performance continued to rise. The total wall-clock time for the 34 epochs executed was approximately 440 h (seed 42).

Model selection was based exclusively on validation performance under greedy decoding. Final test-set evaluation was performed on the selected checkpoint using the three inference modes described in Section 5.3.

To assess the feasibility of real-time on-board deployment, all reported inference latencies reflect single-instance end-to-end processing (batch size 1)—including data transfer, environment construction, and neural forward pass—with explicit device synchronization, reporting the median over the 1,000 test instances. Classical heuristic baselines were executed sequentially on the CPU; neural inference used GPU acceleration. Detailed latency results are reported in Section 6.3.

6. Results and Discussion

All metrics reported in this section are computed exclusively on the 1,000 unseen test instances, which were held out during both training and hyperparameter selection.

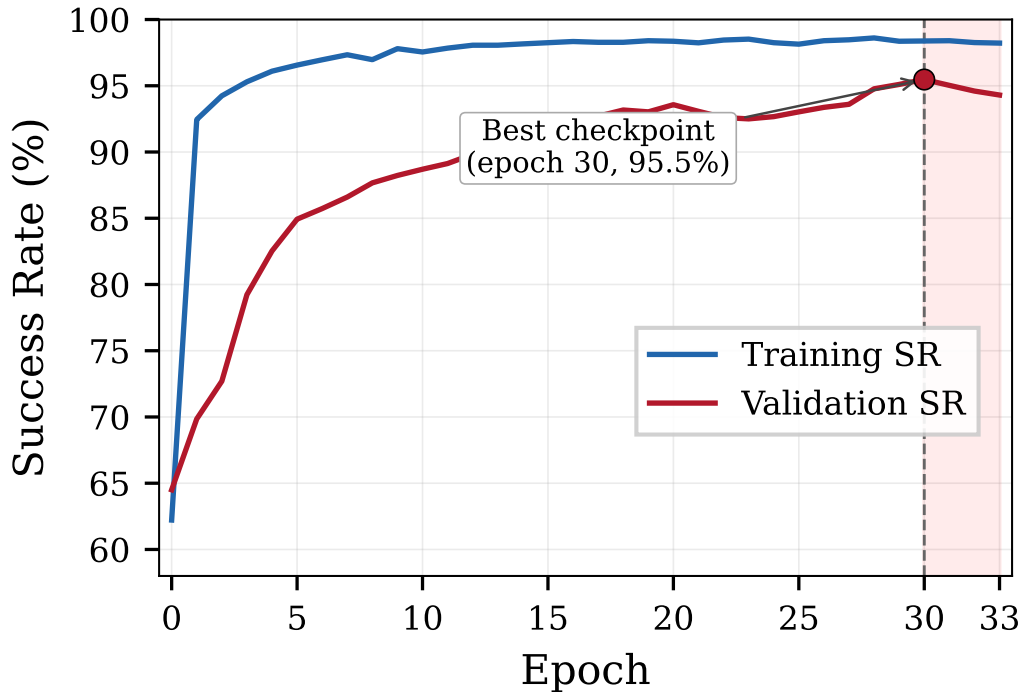


Figure 4: Training and validation success rate (greedy decoding) across epochs. The dashed line marks the selected checkpoint (epoch 30, val. SR = 95.5%). The shaded region indicates overfitting, where validation performance declines while training performance remains stable.

6.1. Coverage performance and feasibility

Table 4 reports the Hamiltonian Success Rate (HSR), Coverage Completion Rate (CCR), and mean node revisits for every evaluated method. Two structural patterns emerge immediately.

First, all 12 revisit-allowed heuristics achieve 100% CCR by design: when a geometric dead-end is encountered, they backtrack or fly back through previously visited cells, trading path efficiency for coverage guarantees. However, *none* of these heuristics produces a Hamiltonian (zero-revisit) path on any test instance with the sole exception of `DFS_Backtrack`, which achieves HSR = 33.8%. This confirms that on irregular hex grids with obstacles, achieving strict single-visit coverage is a qualitatively harder objective than relaxed coverage.

Second, `Warnsdorff`, the only heuristic explicitly designed for Hamiltonian-like traversal, achieves HSR = CCR = 46.0%. Because it forbids revisits, every failure is simultaneously a coverage failure. This 46% solve rate on non-trivial hex topologies establishes the state-of-the-art for greedy construction heuristics in our setting.

Fig. 4 shows the evolution of training and validation success rates across epochs. The policy reaches near-saturation training performance (>98%) within the first 12 epochs, while validation performance converges more gradually. Beyond epoch 30, validation SR begins to decline while training SR continues to increase marginally, confirming standard overfitting behavior and validating the early-stopping criterion.

Against this landscape, the proposed RL policy delivers a qualitative leap. Under greedy de-

coding alone, RL-Greedy achieves HSR = 95.7%, more than double the best heuristic. Stochastic Best-of-16 sampling (RL-BoK16) raises this to 98.7%, and the addition of adjacency-aware 2-opt refinement (RL-BoK16+2opt) reaches 99.0%, within 1% of the theoretical oracle (Exact_DFS, HSR = 100%). All three RL variants achieve zero revisits on every solved instance, confirming that the action-masking mechanism (Section 3.6) enforces strict Hamiltonian feasibility by construction.

The progression from 95.7% to 99.0% across the three inference modes illustrates the value of stochastic sampling and local refinement at test time: sampling explores alternative branching decisions in topologically challenging instances, and 2-opt untangles residual crossings without breaking adjacency constraints. Manual inspection of the 10 failed instances reveals a consistent topological pattern: all exhibit internal obstacles that partition the AOI into sub-regions connected by narrow corridors (one or two cells wide). In every case, the policy successfully covers one sub-region but, in doing so, exhausts the cells forming the connecting passage, leaving the remaining sub-region unreachable. This sequencing failure arises because the optimal visitation order requires committing to a globally non-obvious entry, exit sequence through the bottleneck, a long-horizon planning challenge that the local attention mechanism and 16 stochastic samples are insufficient to resolve. Increasing the sampling budget K or incorporating explicit graph-connectivity lookahead into the decoder are potential mitigations for future work

Table 4: Coverage performance on 1,000 unseen test instances. HSR: Hamiltonian Success Rate (strict single-visit). CCR: Coverage Completion Rate (revisits permitted). Methods are grouped by type and sorted by HSR within each group.

Type	Method	HSR (%)	CCR (%)	Revisits $\mu \pm \sigma$
Oracle	Exact_DFS	100.0	100.0	0.0 \pm 0.0
RL (ours)	RL-BoK16+2opt	99.0	99.0	0.0 \pm 0.0
	RL-BoK16	98.6	98.6	0.0 \pm 0.0
	RL-Greedy	95.7	95.7	0.0 \pm 0.0
Heuristic	Warnsdorff	46.0	46.0	0.0 \pm 0.0
	DFS_Backtrack	33.8	100.0	3.2 \pm 6.0
	Sweep_Boustrophedon	0.0	100.0	6.4 \pm 2.0
	Sweep_Segment_Snake	0.0	100.0	6.5 \pm 2.1
	Sweep_Row_OneWay	0.0	100.0	8.5 \pm 3.4
	Boundary_Spiral_outward	0.0	100.0	12.3 \pm 12.6
	Boundary_Spiral_inward	0.0	100.0	12.4 \pm 12.7
	Sweep_Segment_Interleave	0.0	100.0	16.0 \pm 4.1
	Sweep_Boundary_Peel	0.0	100.0	16.2 \pm 12.5
	Morton_Zorder	0.0	100.0	18.5 \pm 5.4
	Sweep_Row_Interleave	0.0	100.0	18.4 \pm 4.2
	STC_Tree_Coverage	0.0	100.0	35.8 \pm 3.5
	STC_like	0.0	100.0	35.8 \pm 3.5

6.2. Path quality analysis

To compare route quality independently of feasibility differences, distance and turn metrics are computed on the *pairwise common solved subset* $\mathcal{I}_{\cap}^{(m)}$ between each method m and the ref-

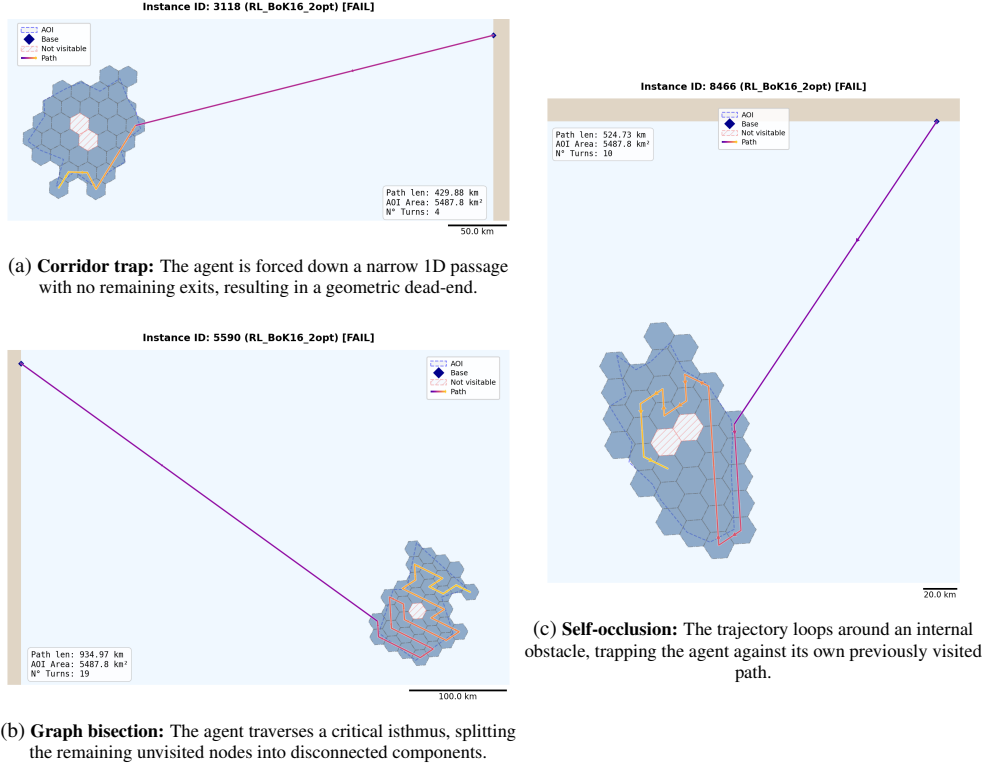


Figure 5: Failure mode analysis of the proposed RL-BoK16+2opt policy. In the rare instances (approx. 1.0%) where the stochastic sampling fails to secure a strict single-visit Hamiltonian path, the failures consistently correspond to severe geometric constraints. As illustrated, these include (a) dead-ends in narrow 1D corridors, (b) topological bisections that isolate clusters of unvisited nodes, and (c) self-occlusion when wrapping around obstacles. In these configurations, the agent commits to a sub-optimal branch that leaves remaining nodes unreachable without revisiting cells, thereby triggering the early dead-end penalty. These edge cases highlight the fundamental fragility of strictly Hamiltonian routing on highly irregular grids and strongly motivate future operational extensions that incorporate a bounded node-revisitation budget.

erence solver RL-BoK16+2opt, which solved 990 of 1,000 test instances. Table 5 summarizes these results.

Distance. RL-BoK16+2opt achieves the lowest mean normalized distance (3.100 ± 0.315) across all 990 common instances, outperforming every heuristic and the oracle DFS. The best heuristic, Warnsdorff (3.328 ± 0.381), is 7.4% longer, but is only comparable on 453 instances due to its low solve rate. Among full-coverage heuristics, the best performer is DFS_Backtrack (3.340 ± 0.449), 7.7% longer than the RL policy. The most commonly deployed survey pattern, Boustrophedon (3.564 ± 0.429), incurs 15.0% more distance. At the extreme, the spanning-tree methods (STC) produce paths 49% longer than the RL solution.

The 2-opt refinement provides a modest but consistent distance improvement over raw sampling: RL-BoK16+2opt is 0.4% shorter than RL-BoK16 (3.111 ± 0.314). Greedy decoding and

Best-of-16 produce identical mean distances, confirming that stochastic sampling primarily improves feasibility rather than path geometry.

Turns. The RL policy produces dramatically smoother paths. RL-BoK16 achieves the fewest turns (32.2 ± 4.7), 25.9% fewer than the best heuristic Warnsdorff (42.5 ± 5.6) and 37.6% fewer than Boustrophedon (51.6 ± 6.6). This reduction is a direct consequence of the continuous turn penalty $f(\theta)$ in the reward function (Equation 7), which the policy internalizes to produce kinematically smooth trajectories. The 2-opt refinement increases turns slightly (34.1 ± 5.2) relative to raw BoK because segment reversals can introduce heading changes while reducing distance—a classical distance–turns trade-off in 2-opt optimization on constrained graphs.

Revisits. All three RL variants achieve exactly zero revisits by construction (action masking forbids revisits). Among heuristics, the cost of guaranteed coverage ranges from 3.2 revisits (DFS_Backtrack) to 35.8 (STC), which translates to 8–95% redundant motion. This redundancy represents wasted fuel and endurance in maritime operations, a cost entirely avoided by the RL policy.

Table 5: Path quality on the pairwise common solved subset with RL-BoK16+2opt (990 of 1,000 test instances solved). n denotes the number of instances solved by *both* the listed method and the RL reference. Methods sorted by normalized distance.

Type	Method	n	Dist. $\mu \pm \sigma$	Turns $\mu \pm \sigma$	Steps	Revisits
RL	RL-BoK16+2opt	991	3.100 ± 0.314	34.1 ± 5.2	37.8	0.0
	RL-BoK16	986	3.110 ± 0.315	32.2 ± 4.7	37.8	0.0
	RL-Greedy	957	3.111 ± 0.314	32.9 ± 4.9	37.8	0.0
Oracle	Exact_DFS	990	3.308 ± 0.374	43.5 ± 6.7	37.8	0.0
Heuristic	Warnsdorff	454	3.325 ± 0.379	42.5 ± 5.6	37.2	0.0
	DFS_Backtrack	990	3.340 ± 0.449	49.5 ± 12.4	41.1	3.2
	Sweep_Boustrophedon	990	3.564 ± 0.429	51.6 ± 6.6	44.2	6.4
	Sweep_Segment_Snake	990	3.567 ± 0.430	51.7 ± 6.5	44.3	6.5
	Sweep_Row_OneWay	990	3.672 ± 0.484	54.4 ± 6.9	46.3	8.5
	Boundary_Spiral_inward	990	3.864 ± 0.772	51.3 ± 19.1	50.3	12.5
	Sweep_Boundary_Peel	990	3.866 ± 0.731	60.0 ± 17.8	54.0	16.2
	Boundary_Spiral_outward	990	3.867 ± 0.765	51.1 ± 18.2	50.1	12.3
	Sweep_Segment_Interl.	990	3.981 ± 0.565	60.9 ± 8.0	53.8	16.0
	Sweep_Row_Interleave	990	4.058 ± 0.554	54.1 ± 7.4	56.2	18.4
	Morton_Zorder	990	4.134 ± 0.620	72.5 ± 9.7	56.2	18.4
	STC_Tree_Coverage	990	4.622 ± 0.721	76.0 ± 12.9	73.6	35.8
	STC_like	990	4.622 ± 0.721	78.8 ± 12.0	73.6	35.8

6.3. Computational efficiency

Table 6 reports per-instance end-to-end inference latencies measured as described in Section 5.5.

Among the heuristics, simple graph-based methods (Warnsdorff, STC) execute sequentially on the CPU in under 1 ms, while sweep-family methods that require geometric axis-selection subproblems take 27–31 ms. In contrast, the RL policy leverages GPU acceleration. Under

Table 6: Per-instance inference latency (ms). Heuristics run on CPU; RL methods on GPU (RTX 3070). Latencies are for inference only, excluding I/O.

Method	ms/instance
Warnsdorff	0.4
STC_Tree_Coverage	0.4
STC_like	0.4
DFS_Backtrack	0.6
Morton_Zorder	0.7
Boundary_Spiral_inward	1.1
Boundary_Spiral_outward	1.2
Sweep_Boundary_Peel	0.7
Sweep_Segment_Snake	26.7
Sweep_Boustrophedon	27.1
Sweep_Row_OneWay	29.2
Sweep_Row_Interleave	29.8
Sweep_Segment_Interl.	31.5
RL-Greedy (GPU)	30.6
RL-BoK16 (GPU)	31.2
RL-BoK16+2opt (GPU)	32.2

greedy decoding, the neural forward pass requires 30.6 ms per instance. While this is comparable to the slower CPU heuristics, the neural policy is solving a strictly harder, tightly constrained Hamiltonian path problem rather than a relaxed coverage sweep. Crucially, Best-of-16 sampling adds only 0.6 ms over the greedy baseline (31.2 ms total) because all 16 rollouts are processed simultaneously in a single batched GPU operation. The subsequent 2-opt refinement adds a further 1.0 ms (32.2 ms total), as its $O(n^2)$ inner loop over short paths ($|\mathcal{V}| \leq 46$) is highly optimized via Numba JIT compilation.

Although comparing CPU-bound heuristics with GPU-accelerated neural policies involves different hardware paradigms, it accurately reflects modern operational realities. Modern autonomous surface vehicles are increasingly equipped with edge AI accelerators (e.g., NVIDIA Jetson modules) designed specifically to host such neural workloads. At approximately 32 ms per instance, all three RL inference modes operate orders of magnitude faster than the typical decision and replanning cycles of maritime autonomous systems, which range from seconds to minutes, fully validating the feasibility of real-time on-board deployment.

6.4. Qualitative path visualization

Fig. 6 presents a comparative visualization of selected methods on representative test instances. The instances were chosen to illustrate three characteristic scenarios: (a) a compact AOI with a central obstacle, (b) an elongated corridor with narrow passages, and (c) an irregular shape with multiple peninsulas.

Across all scenarios, the RL policy produces visually smoother trajectories with fewer sharp heading changes, consistent with the quantitative turn reduction reported in Section 6.2. The Boustrophedon pattern, while achieving complete coverage, exhibits the characteristic zigzag structure with frequent 180° reversals. Warnsdorff produces relatively smooth paths when it succeeds, but fails entirely on instances (b) and (c) where narrow passages create topological

traps. The STC methods produce the most redundant paths, with extensive backtracking visible as dense, overlapping segments. Overall, these qualitative visualizations consistently reflect the quantitative trends observed across the entire 1,000-instance test set, confirming the RL policy’s superior ability to adapt to complex maritime topologies without relying on redundant motion.

6.5. Study limitations

The present study should be interpreted with three scope limitations in mind. First, the proposed RL policy is optimized for the strict no-revisit Hamiltonian formulation, whereas most classical baselines are naturally designed for revisit-allowed complete coverage. For this reason, Hamiltonian feasibility and relaxed coverage completion are reported separately, and route-quality metrics are evaluated conditionally on common solved subsets.

Second, the experiments are conducted on a large synthetic dataset of irregular maritime AOIs. Although the generator is calibrated to operationally meaningful area scales, obstacle densities, and offshore base distances, transfer to real nautical charts with shoreline artifacts, bathymetric constraints, and sensor uncertainty remains to be validated.

Third, the training results reported here correspond to a single full training run due to the substantial computational cost of the end-to-end DRL pipeline. Consequently, the reported uncertainty reflects test-set variability rather than run-to-run optimization variability. Extending the study to multiple independent training seeds is a natural next step for future work.

7. Conclusion and Future Work

This paper introduced a Deep Reinforcement Learning framework for Maritime Coverage Path Planning on irregular hexagonal grids. By framing the problem as a neural combinatorial optimization task and training a Transformer-based pointer policy via a critic-free Group-Relative Policy Optimization (GRPO) scheme, we bypassed the limitations of classical geometric decomposition methods. The incorporation of an early dead-end detection mechanism via BFS significantly sharpened credit assignment during training.

Extensive benchmarking over 1,000 unseen irregular test areas demonstrates that the learned policy, particularly under Best-of-16 sampling with adjacency-aware 2-opt refinement (RL-BoK16+2opt), achieves a 99.0% Hamiltonian success rate, more than doubling the best classical heuristic (46.0%) while producing paths 7% shorter and with up to 24% fewer heading changes than the closest comparable baseline, all with zero node revisits. Inference latency of approximately 32 ms per instance on a laptop GPU confirms the viability of real-time on-board deployment on modern autonomous maritime platforms.

Several extensions of this work merit investigation. First, *non-uniform coverage priorities* can be incorporated by activating the `hexscore` field already embedded in the node features, enabling time-critical surveillance where high-value zones (e.g., distress areas informed by drift models) are visited preferentially. Second, *multi-platform coordination* can be addressed by partitioning the AOI graph and assigning sub-tours to heterogeneous assets, extending the single-agent formulation to multi-agent fleet-level planning. Third, *node revisitation* under a time budget, architecturally supported but not evaluated in the present study, could improve coverage robustness on highly constrained topologies where strict single-visit Hamiltonian paths are fragile. Fourth, *scaling to larger AOIs* (e.g., hyper-resolution maritime grids with 100+ cells) will involve exploring architectural variants, such as alternative attention mechanisms, sparse graph representations, or region-level hierarchical decomposition, to further accelerate training and inference. Finally, *validation on real maritime charts* (e.g., Chilean archipelago coastlines) and

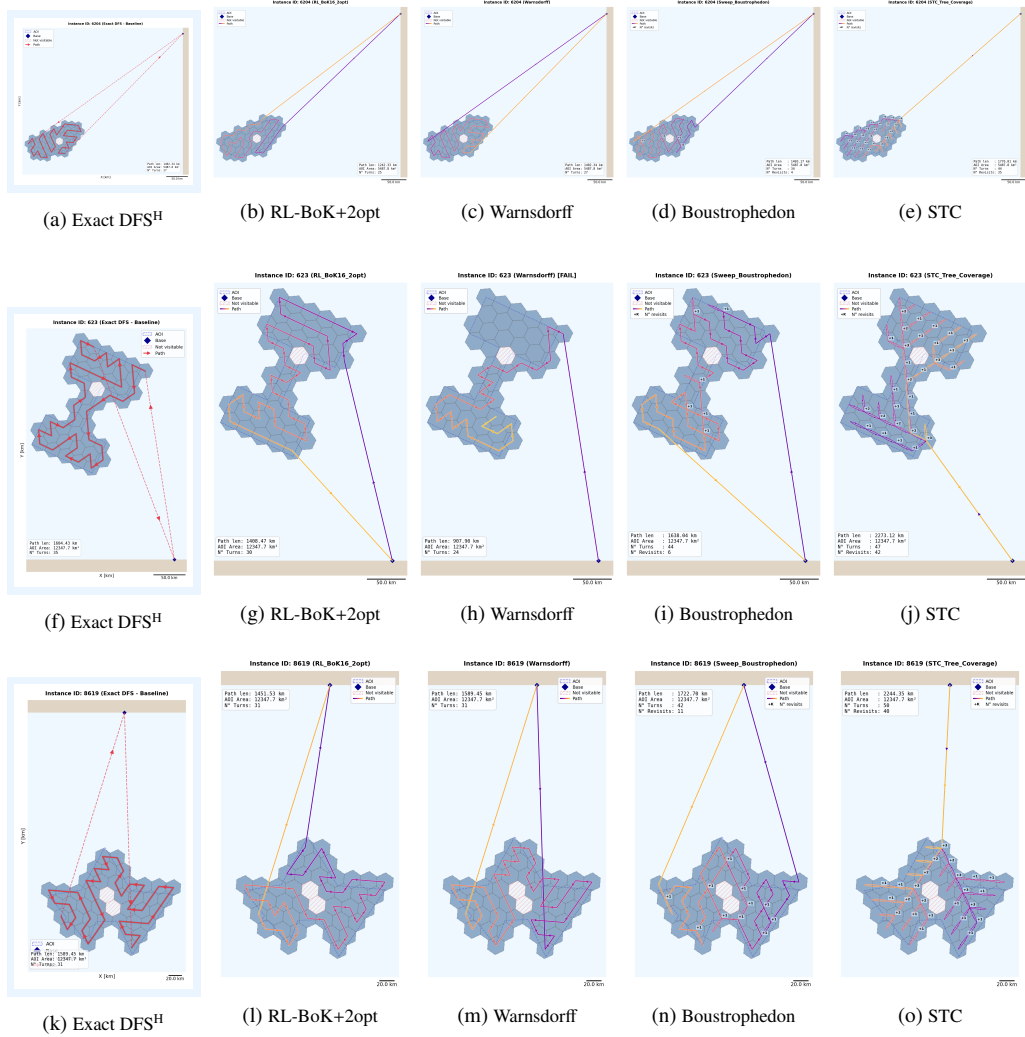


Figure 6: Comparative path visualizations across three representative maritime topologies. The leftmost column (highlighted in blue) displays the Exact DFS (denoted by ^H for Hamiltonian) serving as a topological feasibility oracle. Row 1 shows a small open-water configuration where all methods succeed, though STC introduces dense overlaps. Row 2 presents an H-shaped coastal corridor; here, the RL policy achieves a smooth trajectory, whereas greedy local heuristics like Warnsdorff fail to escape the resulting geometric dead-end. Row 3 illustrates a generic irregular shape, where the RL policy successfully identifies a valid single-visit sequence that avoids the costly kinematic reversals typical of Boustrophedon sweeps.

deployment on autonomous surface vehicles under realistic oceanographic conditions and sensor models represent the natural applied extension of this framework toward operational Maritime Domain Awareness.

CRedit authorship contribution statement

Carlos S. Sepúlveda: Conceptualization, Methodology, Software, Formal analysis, Investigation, Writing – original draft, Writing – review & editing. **Gonzalo A. Ruz:** Supervision, Validation, Writing – review & editing.

Declaration of competing interest

The authors declare that they have no known competing financial interests or personal relationships that could have appeared to influence the work reported in this paper.

Data availability

The synthetic dataset and trained model checkpoint used in this study will be made available upon reasonable request to the corresponding author. Evaluation scripts and baseline implementations will be released in a public repository upon acceptance.

Acknowledgments

This work is also supported by the Chilean Navy through the Directorate of Programs, Research and Development (Armada de Chile), which provided the necessary time and authorization for the development of this research. The authors thank ANID FONDECYT 1230315, ANID-MILENIO-NCN2024_103, ANID-MILENIO-NCN2024_047, and Centro de Modelamiento Matemático (CMM) FB210005, BASAL funds for centers of excellence from ANID-Chile, and the ANID Doctorado Nacional Scholarship, grant number 21210465.

Appendix A. Taxonomy of Surveillance and Routing Problems

Table A.7 summarizes the main families of coverage, patrolling, and routing problems underpinning our approach.

References

- Ai, B., Jia, M., Xu, H., Xu, J., Wen, Z., Li, B., Zhang, D., 2021. Coverage path planning for maritime search and rescue using reinforcement learning. *Ocean Engineering* 241. doi:10.1016/j.oceaneng.2021.110098.
- Alpdemir, M.N., 2022. Tactical uav path optimization under radar threat using deep reinforcement learning. *Neural Computing and Applications* 34, 5649–5664.
- Azad, A.S., Islam, M.M., Chakraborty, S., 2017. A heuristic initialized stochastic memetic algorithm for mdpvrp with interdependent depot operations. *IEEE Transactions on Cybernetics* 47, 4302–4315. doi:10.1109/TCYB.2016.2607220.

Table A.7: Taxonomy of surveillance-related coverage, patrolling, and routing problems underpinning our CPP formulation on hexagonal grids.

Family	Typical objective and common formulation	Relation to this work and representative references
<i>Region coverage (CPP)</i>	Achieve complete coverage of a known area of interest (AOI) while minimising path length, time, or energy. Classical CPP uses cellular decompositions (boustrophedon, trapezoidal, convex) and sweep patterns (e.g., lawnmower), extended to multi-robot and UAV settings.	Our hexagonal AOI discretisation is a discrete CPP formulation in which each hex cell represents a region of the maritime AOI. We follow CPP surveys in robotics and UAVs (Choset, 2001; Galceran and Carreras, 2013; Cabreira et al., 2019; Fevgas et al., 2022) and connect to hex-based CPP and SAR planning in maritime contexts (Azpúrua et al., 2018; Cho et al., 2021b; Kadioglu et al., 2019).
<i>Sweep and barrier coverage</i>	Ensure that every point of a region or a virtual barrier is periodically visited by mobile sensors, subject to revisit intervals or detection constraints. Models often rely on TSP/graph tours, Eulerian paths, or approximation algorithms for large-scale sweep coverage and barrier placement.	When maritime AOIs degenerate into corridors (routes, shorelines, chokepoints), our hex-grid CPP reduces to sweep or barrier-type problems over 1D/2D structures. Sweep-coverage and barrier-coverage results in WSNs (Li et al., 2011; Gorain and Mandal, 2014; Benahmed and Benahmed, 2019; Nguyen and So-In, 2018; Li et al., 2019; Kong et al., 2016) motivate modeling “barriers” or critical routes via specialized boundary constraints and periodic revisit scheduling.
<i>Patrolling and persistent surveillance</i>	Maintain high-quality surveillance over long horizons by minimizing maximal idle time, maximizing information gain, or enforcing revisit-frequency constraints under vehicle range and kinematic limitations. Formulations often use infinite-horizon control or MILP-based routing with information metrics.	Weighted coverage objective can be interpreted as a single-visit proxy for persistent-surveillance value on hex-grids. Patrolling and persistent-surveillance works with UAVs and surface vehicles (Nigam et al., 2009; Zuo et al., 2020; Bandarupalli et al., 2021; Savkin and Huang, 2019; Luis et al., 2020, 2021) motivate the use of information-based metrics that could inform future extensions with non-uniform priorities.
<i>Routing for surveillance and mission planning</i>	Plan routes for one or multiple platforms that visit regions or tasks while minimizing mission cost (time, fuel) and respecting range, time windows, and motion constraints. Typical formulations are TSP/VRP variants, orienteering, and Dubins-type routing, often solved via MILP or heuristics.	Our approach inherits the routing structure of maritime surveillance mission-planning models: hex cells act as “customers” to be visited, and tours must satisfy sensor and endurance constraints. Classical radar/SAR routing and UAV mission-planning work (Panton and Elbers, 1999; John et al., 2001; Grob, 2006; Karasakal, 2016; Coutinho et al., 2018; Otto et al., 2018; Cho et al., 2021b,a) serve as baselines to benchmark our learned policies.
<i>Spatial crowdsourcing and task assignment</i>	Assign spatial sensing or monitoring tasks to agents (humans, vehicles, sensors) to maximise utility or coverage subject to capacity, location, and temporal constraints. Models are often matching or assignment problems with uncertainty in agent availability and task locations.	In multi-platform maritime surveillance, our hex-based CPP can be extended with task-assignment layers that allocate subsets of hex cells or sub-tours to heterogeneous assets. Spatial crowdsourcing and mobile-sensing literature (Wu et al., 2019; Bhatti et al., 2021; Tong et al., 2020; Zhou et al., 2019; Chen et al., 2020) informs potential extensions where different vehicles or sensor types share the same

- Azpúrua, H., Freitas, G.M., Macharet, D.G., Campos, M.F., 2018. Multi-robot coverage path planning using hexagonal segmentation for geophysical surveys. *Robotica* 36, 1144–1166. doi:10.1017/S0263574718000292.
- Bähnemann, R., Lawrance, N., Chung, J.J., Pantic, M., Siegwart, R., Nieto, J., 2021. Revisiting boustrophedon coverage path planning as a generalized traveling salesman problem, in: *Field and Service Robotics: Results of the 12th International Conference*, Springer. pp. 277–290.
- Bandarupalli, A., Swarup, D., Weston, N., Chaterji, S., 2021. Persistent airborne surveillance using semi-autonomous drone swarms, in: *Proceedings of the 7th Workshop on Micro Aerial Vehicle Networks, Systems, and Applications*, pp. 19–24. doi:10.1145/3469259.3470487.
- Bello, I., Pham, H., Le, Q.V., Norouzi, M., Bengio, S., 2016. Neural combinatorial optimization with reinforcement learning. *5th International Conference on Learning Representations, ICLR 2017 - Workshop Track Proceedings* .
- Benahmed, T., Benahmed, K., 2019. Optimal barrier coverage for critical area surveillance using wireless sensor networks. *International Journal of Communication Systems* 32. doi:10.1002/dac.3955.
- Berto, F., Hua, C., Park, J., Luttmann, L., Ma, Y., Bu, F., Wang, J., Ye, H., Kim, M., Choi, S., et al., 2025. RI4co: an extensive reinforcement learning for combinatorial optimization benchmark, in: *Proceedings of the 31st ACM SIGKDD Conference on Knowledge Discovery and Data Mining V. 2*, pp. 5278–5289.
- Bhatti, S.S., Fan, J., Wang, K., Gao, X., Wu, F., Chen, G., 2021. An approximation algorithm for bounded task assignment problem in spatial crowdsourcing. *IEEE Transactions on Mobile Computing* 20, 2536–2549. doi:10.1109/TMC.2020.2984380.
- Biniarz, A., Liu, P., Maheshwari, A., Smid, M., 2017. Approximation algorithms for the unit disk cover problem in 2d and 3d. *Computational Geometry* 60, 8–18. doi:10.1016/J.COMGEO.2016.04.002.
- Bischof, Z.S., Fontugne, R., Bustamante, F.E., 2018. Untangling the world-wide mesh of under-sea cables, in: *Proceedings of the 17th ACM workshop on hot topics in networks*, pp. 78–84.
- Boots, B., Okabe, A., Sugihara, K., 1999. Spatial tessellations, in: *Geographical Information Systems*, pp. 503–526.
- Boraz, S.C., 2009. Maritime domain awareness: Myths and realities. *Naval War College Review* 62, 137–146. doi:10.2307/26397039.
- Bueger, C., Edmunds, T.P., Stockbruegger, J., 2024. *Securing the seas: A comprehensive assessment of global maritime security* .
- Cabreira, T.M., Brisolara, L.B., Paulo, R.F., 2019. Survey on coverage path planning with unmanned aerial vehicles. *Drones* 3, 1–38. doi:10.3390/drones3010004.
- Chen, C.C., Chang, C.Y., Chen, P.Y., 2015. Linear time approximation algorithms for the relay node placement problem in wireless sensor networks with hexagon tessellation. *Journal of Sensors* 2015. doi:10.1155/2015/565983.

- Chen, M., Wang, T., Ota, K., Dong, M., Zhao, M., Liu, A., 2020. Intelligent resource allocation management for vehicles network: An a3c learning approach. *Computer Communications* 151, 485–494. doi:10.1016/J.COMCOM.2019.12.054.
- Cho, S.W., Park, H.J., Lee, H., Shim, D.H., Kim, S.Y., 2021a. Coverage path planning for multiple unmanned aerial vehicles in maritime search and rescue operations. *Computers and Industrial Engineering* 161. doi:10.1016/j.cie.2021.107612.
- Cho, S.W., Park, J.H., Park, H.J., Kim, S., 2021b. Multi-uav coverage path planning based on hexagonal grid decomposition in maritime search and rescue. *Mathematics* 10, 83.
- Choi, Y., Choi, Y., Briceno, S., Mavris, D.N., 2019. Multi-uas path-planning for a large-scale disjoint disaster management, in: *2019 International Conference on Unmanned Aircraft Systems (ICUAS)*, pp. 799–807.
- Choi, Y., Choi, Y., Briceno, S., Mavris, D.N., 2020. Energy-constrained multi-uav coverage path planning for an aerial imagery mission using column generation. *Journal of Intelligent & Robotic Systems* 97, 125–139.
- Choset, H., 2001. Coverage for robotics—a survey of recent results. *Annals of mathematics and artificial intelligence* 31, 113–126.
- Coutinho, W.P., Battarra, M., Fliege, J., 2018. The unmanned aerial vehicle routing and trajectory optimisation problem, a taxonomic review. *Computers & Industrial Engineering* 120, 116–128. doi:10.1016/J.CIE.2018.04.037.
- Darvari, V.A., Hailes, S., Musolesi, M., 2024. Graph reinforcement learning for combinatorial optimization: A survey and unifying perspective. *arXiv preprint arXiv:2404.06492*.
- Dogancay, K., Tu, Z., Ibal, G., 2021. Research into vessel behaviour pattern recognition in the maritime domain: Past, present and future. *Digital Signal Processing* 119, 103191. doi:10.1016/J.DSP.2021.103191.
- Fevgas, G., Lagkas, T., Argyriou, V., Sarigiannidis, P., 2022. Coverage path planning methods focusing on energy efficient and cooperative strategies for unmanned aerial vehicles. *Sensors* 22. doi:10.3390/s22031235.
- Galceran, E., Carreras, M., 2013. A survey on coverage path planning for robotics. *Robotics and Autonomous systems* 61, 1258–1276.
- Gao, M., Kang, Z., Zhang, A., Liu, J., Zhao, F., 2022. Mass autonomous navigation system based on ais big data with dueling deep q networks prioritized replay reinforcement learning. *Ocean Engineering* 249. doi:10.1016/J.OCEANENG.2022.110834.
- Gorain, B., Mandal, P.S., 2014. Approximation algorithms for sweep coverage in wireless sensor networks. *Journal of parallel and Distributed Computing* 74, 2699–2707.
- Grob, M.J., 2006. Routing of platforms in a maritime surface surveillance operation. *European Journal of Operational Research* 170, 613–628. doi:10.1016/j.ejor.2004.02.029.
- Huang, S., Ontañón, S., 2022. A closer look at invalid action masking in policy gradient algorithms, in: *The International FLAIRS Conference Proceedings*.

- Islam, K., Meijer, H., Rodríguez, Y.N., Rappaport, D., Xiao, H., 2007. Hamilton circuits in hexagonal grid graphs., in: CCCG, pp. 85–88.
- John, M., Panton, D., White, K., 2001. Mission planning for regional surveillance. *Annals of Operations Research* 108, 157–173.
- Kadioglu, E., Urtis, C., Papanikolopoulos, N., 2019. Uav coverage using hexagonal tessellation, in: 27th Mediterranean Conference on Control and Automation, MED 2019 - Proceedings, Institute of Electrical and Electronics Engineers Inc.. pp. 37–42. doi:10.1109/MED.2019.8798564.
- Kaelbling, L.P., Littman, M.L., Moore, A.W., 1996. Reinforcement learning: A survey. *Journal of Artificial Intelligence Research* 4, 237–285. doi:10.1613/JAIR.301.
- Karapetyan, N., Braude, A., Moulton, J., Burstein, J.A., White, S., O’Kane, J.M., Rekleitis, I., 2019. Riverine coverage with an autonomous surface vehicle over known environments, in: 2019 IEEE/RSJ International Conference on Intelligent Robots and Systems (IROS), IEEE. pp. 3098–3104.
- Karasakal, O., 2016. Minisum and maximin aerial surveillance over disjoint rectangles. *Top* 24, 705–724. doi:10.1007/s11750-016-0416-1.
- Kong, L., Lin, S., Xie, W., Qiao, X., Jin, X., Zeng, P., Ren, W., Liu, X.Y., 2016. Adaptive barrier coverage using software defined sensor networks. *IEEE Sensors Journal* 16, 7364–7372. doi:10.1109/JSEN.2016.2566808.
- Kool, W., Hoof, H.V., Welling, M., 2018. Attention, learn to solve routing problems! arXiv preprint arXiv:1803.08475 .
- Kumar, K., Kumar, N., 2023. Region coverage-aware path planning for unmanned aerial vehicles: A systematic review. *Physical Communication* 59, 102073. doi:10.1016/J.PHYCOM.2023.102073.
- Kwon, Y.D., Choo, J., Kim, B., Yoon, I., Gwon, Y., Min, S., 2020. Pomo: Policy optimization with multiple optima for reinforcement learning. *Advances in Neural Information Processing Systems* 33, 21188–21198.
- Li, J., Ma, Y., Gao, R., Cao, Z., Lim, A., Song, W., Zhang, J., 2021a. Deep reinforcement learning for solving the heterogeneous capacitated vehicle routing problem. *IEEE Transactions on Cybernetics* 54, 13572–13585. doi:10.1109/TCYB.2021.3111082.
- Li, J., Xin, L., Cao, Z., Lim, A., Song, W., Zhang, J., 2021b. Heterogeneous attentions for solving pickup and delivery problem via deep reinforcement learning. *IEEE TRANSACTIONS ON INTELLIGENT TRANSPORTATION SYSTEMS* .
- Li, J., Xiong, Y., She, J., Wu, M., 2020. A path planning method for sweep coverage with multiple uavs. *IEEE Internet of Things Journal* 7, 8967–8978. doi:10.1109/JIOT.2020.2999083.
- Li, L., Chen, H., 2022. Uav enhanced target-barrier coverage algorithm for wireless sensor networks based on reinforcement learning. *Sensors* 22, 6381. doi:10.3390/S22176381.

- Li, M., Cheng, W., Liu, K., Liu, Y., Li, X., Liao, X., Lab, W.J., 2011. Sweep coverage with mobile sensors. *IEEE Transactions on Mobile Computing* 10, 1534–1545.
- Li, S., Shen, H., Huang, Q., Guo, L., 2019. Optimizing the sensor movement for barrier coverage in a sink-based deployed mobile sensor network. *IEEE Access* 7, 156301–156314. doi:10.1109/ACCESS.2019.2949025.
- Li, X., Savkin, A.V., 2021. Networked unmanned aerial vehicles for surveillance and monitoring: A survey. *Future Internet* 13. doi:10.3390/FI13070174.
- Liu, Z., Liu, Y., 2021. Agent-based simulation of multi-uav search-track for dynamic targets in sweep coverage, in: *Journal of Physics: Conference Series*, IOP Publishing. p. 012033.
- Luis, S.Y., Reina, D.G., Marín, S.L., 2021. A multiagent deep reinforcement learning approach for path planning in autonomous surface vehicles: The ypacarai lake patrolling case. *IEEE Access* 9, 17084–17099. doi:10.1109/ACCESS.2021.3053348.
- Luis, S.Y., Reina, D.G., Marín, S.L.T., 2020. A deep reinforcement learning approach for the patrolling problem of water resources through autonomous surface vehicles: The ypacarai lake case. *IEEE Access* 8, 204076–204093. doi:10.1109/ACCESS.2020.3036938.
- Mier, G., Valente, J., Bruin, S.D., 2023. Fields2cover: An open-source coverage path planning library for unmanned agricultural vehicles. *IEEE Robotics and Automation Letters* 8, 2166–2172.
- Nazari, M., Oroojlooy, A., Takáč, M., Snyder, L.V., 2018. Reinforcement learning for solving the vehicle routing problem. *Advances in neural information processing systems* 31.
- Nguyen, T.G., So-In, C., 2018. Distributed deployment algorithm for barrier coverage in mobile sensor networks. *IEEE Access* 6, 21042–21052. doi:10.1109/ACCESS.2018.2822263.
- Nielsen, L.D., Sung, I., Nielsen, P., 2019. Convex decomposition for a coverage path planning for autonomous vehicles: Interior extension of edges. *Sensors* 19. doi:10.3390/s19194165.
- Nigam, N., Bieniawski, S., Kroo, I., Vian, J., 2009. Control of multiple uavs for persistent surveillance: Algorithm description and hardware demonstration. *IEEE Transactions on Control Systems Technology* 20, 1236–1251.
- Otto, A., Agatz, N., Campbell, J., Golden, B., Pesch, E., 2018. Optimization approaches for civil applications of unmanned aerial vehicles (uavs) or aerial drones: A survey. *Networks* 72, 411–458. doi:10.1002/NET.21818.
- Panton, D.M., Elbers, A.W., 1999. Mission planning for synthetic aperture radar surveillance. *Interfaces* 29, 73–88. doi:10.1287/inte.29.2.73.
- de Ministros para el desarrollo de una Política Oceánica Nacional, C., 2023. Programa oceánico nacional: Plan oceánico sostenible Chile 2023.
- Raza, S.M., Sajid, M., Singh, J., 2022. Vehicle routing problem using reinforcement learning: Recent advancements, in: *Lecture Notes in Electrical Engineering*, Springer Science and Business Media Deutschland GmbH. pp. 269–280. doi:10.1007/978-981-19-0840-8_20.

- Savkin, A.V., Huang, H., 2019. Proactive deployment of aerial drones for coverage over very uneven terrains: A version of the 3d art gallery problem. *Sensors* 19, 1438. doi:10.3390/S19061438.
- Schulman, J., Wolski, F., Dhariwal, P., Radford, A., Klimov, O., 2017. Proximal policy optimization algorithms. *arXiv preprint arXiv:1707.06347* .
- Shao, Z., Wang, P., Zhu, Q., Xu, R., Song, J., Bi, X., Zhang, H., Zhang, M., Li, Y., et al., 2024. Deepseekmath: Pushing the limits of mathematical reasoning in open language models. *arXiv preprint arXiv:2402.03300* .
- Siew, P.M., Jang, D., Roberts, T.G., Linares, R., Fletcher, J., 2022. Cislunar space situational awareness sensor tasking using deep reinforcement learning agents, in: *2022 Advanced Maui Optical and Space Surveillance Technologies Conference (AMOS)*, Maui, Hawaii.
- Siew, P.M., Linares, R., 2022. Optimal tasking of ground-based sensors for space situational awareness using deep reinforcement learning. *Sensors* 22. doi:10.3390/s22207847.
- Soldi, G., Gaglione, D., Forti, N., Simone, A.D., Daffinà, F.C., Bottini, G., Quattrocioni, D., Millefiori, L.M., Braca, P., Carniel, S., Willett, P., Iodice, A., Riccio, D., Farina, A., 2021. Space-based global maritime surveillance. part i: Satellite technologies. *IEEE Aerospace and Electronic Systems Magazine* 36, 8–28.
- Sutton, R.S., Barto, A.G., 2018. *Reinforcement learning : an introduction*. second edition ed., MIT press.
- Tan, C.S., Mohd-Mokhtar, R., Arshad, M.R., 2021. A comprehensive review of coverage path planning in robotics using classical and heuristic algorithms. *IEEE Access* 9, 119310–119342. doi:10.1109/ACCESS.2021.3108177.
- Tong, Y., Zhou, Z., Zeng, Y., Chen, L., Shahabi, C., 2020. Spatial crowdsourcing: a survey. *VLDB Journal* 29, 217–250. doi:10.1007/S00778-019-00568-7/METRICS.
- United Nations Trade and Development (UNCTAD), 2024. *Review of maritime transport 2024: Navigating maritime chokepoints*. Stylus Publishing, LLC.
- Vinyals, O., Fortunato, M., Jaitly, N., 2015. Pointer networks. *Advances in neural information processing systems* 28.
- Wu, J., Cheng, L., Chu, S., Song, Y., 2024. An autonomous coverage path planning algorithm for maritime search and rescue of persons-in-water based on deep reinforcement learning. *Ocean engineering* 291, 116403.
- Wu, L., Xiong, Y., Wu, M., He, Y., She, J., 2019. A task assignment method for sweep coverage optimization based on crowdsensing. *IEEE Internet of Things Journal* 6, 10686–10699. doi:10.1109/JIOT.2019.2940717.
- Xin, L., Song, W., Cao, Z., Zhang, J., 2021. Multi-decoder attention model with embedding glimpse for solving vehicle routing problems, in: *Proceedings of the AAAI Conference on Artificial Intelligence*, pp. 12042–12049.

- Zelenka, J., Kasanický, T., Bundzel, M., Andoga, R., 2020. Self-adaptation of a heterogeneous swarm of mobile robots to a covered area. *Applied Sciences (Switzerland)* 10. doi:10.3390/app10103562.
- Zhou, Z., Liu, P., Feng, J., Zhang, Y., Mumtaz, S., Rodriguez, J., 2019. Computation resource allocation and task assignment optimization in vehicular fog computing: A contract-matching approach. *IEEE Transactions on Vehicular Technology* 68, 3113–3125. doi:10.1109/TVT.2019.2894851.
- Zuo, Y., Tharmarasa, R., Jassemi-Zargani, R., Kashyap, N., Thiyagalingam, J., Kirubarajan, T.T., 2020. Milp formulation for aircraft path planning in persistent surveillance. *IEEE Transactions on Aerospace and Electronic Systems* 56, 3796–3811. doi:10.1109/TAES.2020.2983532.
- Zweig, A., Ahmed, N., Willke, T.L., Ma, G., 2020. Neural algorithms for graph navigation, in: *Learning Meets Combinatorial Algorithms at NeurIPS2020*.